The FXR1 network acts as signaling scaffold for actomyosin remodeling

Xiuzhen Chen[1], Mervin M. Fansler[1], Urška Janjoš[2,4], Jernej Ule[2,3], and Christine Mayr[1,*]

[1]Cancer Biology and Genetics Program, Sloan Kettering Institute, New York, NY 10065, USA

[2]National Institute of Chemistry, Hajdrihova 19, 1001 Ljubljana, Slovenia

[3]UK Dementia Research Institute at King's College London, London, SE5 9NU, UK

[4]Biosciences PhD Program, Biotechnical Faculty, University of Ljubljana, Ljubljana, Slovenia

[*]Correspondence and Lead Contact: mayrc@mskcc.org

Summary

It is currently not known whether mRNAs fulfill structural roles in the cytoplasm. Here, we report the FXR1 network, an mRNA-protein (mRNP) network present throughout the cytoplasm, formed by FXR1-mediated packaging of exceptionally long mRNAs. These mRNAs serve as underlying condensate scaffold and concentrate FXR1 molecules. The FXR1 network contains multiple protein binding sites and functions as a signaling scaffold for interacting proteins. We show that it is necessary for RhoA signaling-induced actomyosin reorganization to provide spatial proximity between kinases and their substrates. Point mutations in FXR1, found in its homolog FMR1, where they cause Fragile X syndrome, disrupt the network. FXR1 network disruption prevents actomyosin remodeling—an essential and ubiquitous process for the regulation of cell shape, migration, and synaptic function. These findings uncover a structural role for cytoplasmic mRNA and show how the FXR1 RNA-binding protein as part of the FXR1 network acts as organizer of signaling reactions.

Keywords

RNA-binding protein; FXR1; structural role of mRNA; non-canonical roles of mRNA; FMR1; messenger ribonucleoprotein (mRNP) network; biomolecular condensates; cytoplasmic organization; Actomyosin reorganization; signaling scaffold; signal transduction; spatial proximity; protein interaction hub; Fragile X syndrome

Introduction

Cells use biomolecular condensates to generate compartments that are not surrounded by membranes[1]. These compartments are thought to enable the spatial organization of biochemical activities[2]. For example, condensates function as signaling clusters for T cell activation or concentrate factors for the nucleation and assembly of actin filaments[3,4]. Cytoplasmic messenger ribonucleoprotein (mRNP) granules are a group of condensates, formed through self-assembly of mRNAs and their bound proteins. They include P bodies and stress granules

41 and are thought to function in mRNA storage and decay[5,6], where it appears that mRNAs take
42 on passive roles of being stored or degraded. In contrast, within TIS granules, mRNAs actively
43 contribute to protein functions by establishing mRNA-dependent protein complexes[7-9]. An
44 apparent difference between P bodies or stress granules and TIS granules is the network-like
45 morphology of TIS granules, which is generated through RNA-RNA interactions[7,10]. In this study,
46 our goal was to identify another cytoplasmic mRNP network and to investigate whether mRNAs
47 have broader structural or regulatory roles in addition to serving as templates for protein
48 synthesis.

49 We focused our study on FXR1, an RNA-binding protein from the family of Fragile X-related
50 (FXR) proteins[11]. FXR proteins are ancient and were found in invertebrates but have expanded
51 into three family members in vertebrates[11,12]. *FXR1* and *FXR2* are homologs of the *FMR1* gene,
52 whose loss of function causes the most common form of hereditary mental retardation in
53 humans, Fragile X syndrome (FXS)[11,13]. FXR1 has recently also been implicated in neurological
54 disorders, as several genome-wide association studies found variants in *FXR1* that are
55 associated with a higher risk for autism spectrum disorder (ASD), intellectual disability, and
56 schizophrenia[14-17].

57 FXR1 is an essential gene in humans, as loss of function of FXR1 is not tolerated[18]. Whereas
58 mice with knockouts of *FMR1* or *FXR2* are viable, loss of FXR1 results in perinatal lethality,
59 likely due to cardiac or respiratory failure[19]. FXR1 has mostly been studied as a regulator of
60 translation in brain, testis, and muscle[20-22]. However, *FXR1* may have broader roles, as *FXR1* is
61 ubiquitously expressed and was detected among the top 15% of expressed genes in primary
62 fetal and adult cell types (Fig. S1A)[23].

63 Here, we find that the longest expressed mRNAs assemble with FXR1 into a large cytoplasmic
64 mRNP network, which we call the FXR1 network. Only a small fraction of FXR1 is stably bound
65 to mRNA, these FXR1 molecules together with the bound mRNAs act as network scaffold.
66 FXR1 contains multiple protein binding sites, including coiled-coil (CC), Tudor, and RGG
67 domains, which allow the recruitment of most FXR1 molecules as clients into the network, thus
68 generating a high FXR1 concentration. Additional clients, such as signaling molecules with
69 similar protein domains as FXR1 are also recruited to the network, which promotes their
70 proximity. We show that an intact FXR1 network is necessary for RhoA signaling-induced
71 actomyosin reorganization, as it provides proximity between the Rho-associated kinase and its
72 substrates. Actomyosin remodeling is crucial for many cellular processes including the control of
73 cell shape, migration, and synaptic function. Taken together, we demonstrate that mRNAs fulfil
74 structural roles in the cytoplasm. They provide an underlying scaffold for FXR1, whose high
75 concentration of multiple protein binding sites generates a platform for signaling molecules to
76 utilize this mRNP network despite lacking RNA-binding domains.

77

78 **Results**

79 **FXR1 and its bound mRNAs assemble into a large cytoplasmic mRNP network**

80 To identify additional cytoplasmic mRNP networks, we performed a small-scale high-resolution
81 imaging screen on highly abundant cytoplasmic RNA-binding proteins. Using immunostaining,
82 we observed that endogenous FXR1 forms a network-like structure that covers the whole
83 cytoplasm (Fig. 1A). We call this assembly the FXR1 network, which is composed of extensively
84 connected spherical granules (Fig. 1A). The FXR1 network is present in all cells of all eight cell
85 types examined (Fig. S1B) and was also observed in C2C12 myotubes[24].

86 The network-like morphology was also observed with live cell imaging of monomeric
87 NeonGreen (NG)-tagged endogenous FXR1 (Fig. 1B, S1C-G). Both major splice isoforms

88   expressed in non-muscle cells are capable of FXR1 network formation (Fig. S2A-F). The higher-
89   order assembly of FXR1 observed by imaging was confirmed using size-exclusion
90   chromatography (Fig. 1C). FXR1 protein exists predominantly within high-molecular-weight
91   complexes with an estimated size of more than 1,000 kDa. In contrast, monomeric FXR1 is
92   present at very low levels in cells (Fig. 1C).

93

The underlying scaffold of the FXR1 network is RNA

95   To learn how FXR1 assembles into a network, we ectopically expressed monomeric GFP-fused
96   FXR1 and its variants in cells depleted of endogenous FXR1 protein (Fig. S2E). In its N-terminal
97   half, FXR1 protein contains several folded domains that are followed by an intrinsically
98   disordered region (IDR) (Fig. 1D). Expression of the IDR fused to GFP resulted in diffusive
99   signal, similar to that of GFP alone, whereas expression of the folded domains, which contain
100   two KH RNA-binding domains[11], generated spherical granules, different from the full-length
101   FXR1 protein (Fig. 1E). KH domain mutation generated a diffusive signal, indicating that
102   formation of the granules requires RNA binding of FXR1 (Fig. S3A-C).

103   Intriguingly, when fusing the first 20 aa of the IDR with the folded domains of FXR1, the
104   spherical granules turned into a network-like structure (FXR1-N2, Fig. 1E). The first 20 aa of the
105   IDR contain an RG-rich region. RG motifs are known as RNA-binding regions[25], suggesting that
106   RNA may be responsible for connecting the granules and for network formation (Fig. S3C). We
107   tested this prediction by treating the assembled network with RNase A, which reverted the
108   network into spherical granules (Fig. 1F, S3D). Furthermore, mutating the five arginines of the
109   RG motif into alanines abolished its ability to connect the granules. In contrast, substituting the
110   arginines with five positively charged lysine residues retained this activity (Fig. S3C). These
111   results indicate that RNA forms the connections between the spherical granules. Together,
112   these data demonstrate that RNA is essential for both the initial granule formation and their
113   remodeling into a network.

114

The FXR1 network is highly dynamic

116   To better understand the material properties of the FXR1 network, we acquired time lapses and
117   performed fluorescent recovery after photobleaching (FRAP). Full-length FXR1 generates a
118   highly dynamic network, whose components are highly mobile, as over 50% of the initial
119   fluorescence recovered in less than two seconds (Fig. 1G, Videos S1 and S2). In contrast,
120   FXR1-N2 localizes to the perinuclear region, where it forms a rather static assembly, with a low
121   fraction of mobile molecules, according to FRAP (Fig. 1G, Video S3). These results suggest that
122   the IDR is responsible for the high protein mobility in the network. FXR1-N1 generates highly
123   dynamic and mobile granules that rarely fuse upon contact (Figure 1G, Videos S4 and S5).
124   Over twelve hours, their numbers and occupied areas remain quite constant (Fig. S3E, S3F). In
125   the presence of the RG motif however (FXR1-N2), the granule numbers decrease substantially,
126   while their sizes increase (Fig. S3G, S3H), indicating that the RG motif is responsible for the
127   fusion of the granules and network formation.

128

FXR1 dimerization through the CC domains nucleates the FXR1 network

130   Although FXR1 is primarily known as an RNA-binding protein, it also contains multiple domains
131   for protein:protein interactions (Fig. 2A)[11,26,27]. FXR1 contains two Tudor domains, which
132   mediate dimerization and bind to methylated arginines[25,28-30]. The two KH RNA-binding domains
133   have also been reported as protein:protein interaction domains[11,31-34]. The KH0 domain may act

134   as protein:protein interaction domain because it lacks the GXXG motif required for RNA-
135   binding[27]. FXR1 contains two predicted CC domains (Fig. S4A)[26,35]. Within its IDR, there are
136   three arginine-rich regions (RG, RGG, R). RG/RGG motifs are multifunctional as they can bind
137   to RNA or to protein[25,36-38]. They often bind to other RGG motifs, resulting in homo- or
138   heterooligomerization[25,28,29,37-39]. Taken together, FXR1 contains at least five domains for
139   protein:RNA interactions and nine domains capable of forming protein:protein interactions (Fig.
140   2A).

141   To probe the molecular mechanism of FXR1 network assembly, we set out to generate an
142   FXR1 assembly-deficient mutant, while keeping the RNA-binding domains intact. Removal of
143   the Tudor domains resulted in network disruption that was restored upon overexpression (Fig.
144   S3I), suggesting that the Tudor domains are not essential for network assembly. In contrast,
145   intact CC domains are essential to nucleate the FXR1 network (Fig. 2B, 2C). Introduction of a
146   single helix-breaking point mutation in either one of the CC domains was sufficient to fully
147   disrupt the FXR1 network (Fig. 2B, 2C, S4A-D)[40]. Moreover, FXR1 variants that contained only
148   either CC1 or CC2 at both positions could not nucleate the FXR1 network, whereas swapping
149   the CC domains maintained FXR1 network assembly (Fig. 2B, 2C, S4C). These results
150   converge on a model wherein FXR1 network formation requires heteromeric binding of the two
151   CC domains, which is supported by biochemical evidence that intact CC domains are essential
152   for dimerization of FXR1 (Fig. 2D).

153

154   **FXR1 dimerization strongly promotes mRNA binding**

155   Since RNA binding is essential for network assembly (Fig. 1F, Fig. S3A-D), we determined
156   whether FXR1 dimerization affects its mRNA binding capacity. We performed native oligo(dT)
157   pulldown experiments using GFP-tagged wildtype (WT) FXR1 or the CC mutants expressed at
158   levels similar to the endogenous protein (Fig. S2E)[24,41]. Only WT FXR1 stably interacted with
159   mRNA (Fig. 2E). In contrast, mRNA binding of the FXR1 CC mutants was strongly reduced,
160   indicating that monomeric FXR1 is a poor mRNA-binding protein. As swapping the CC domains
161   rescued RNA binding, these data indicate that FXR1 dimerization is required for stable mRNA
162   binding in cells (Fig. 2E). When comparing mRNA binding of FXR1 with that of HuR, we
163   observed that nearly all of HuR was enriched by oligo(dT) pulldown, but only a small fraction of
164   FXR1, estimated to be ~2%, was bound to mRNA (Fig. 2E). mRNA binding to FXR1 enables
165   higher-order assembly of FXR1, as indicated by size exclusion chromatography, which showed
166   that FXR1 with mutated CC domains is predominantly present as monomeric protein in cells
167   (Fig. S4E). These data indicate that FXR1 dimerization is a prerequisite for stable RNA binding.
168   They also suggest that only a minority of FXR1 is stably bound to RNA, whereas most FXR1
169   molecules associate with the network in an RNA-independent manner.

170

171   **FMR1 also forms a large cytoplasmic mRNP network**

172   The FXR family member FMR1 has the same domain architecture as FXR1 (Fig. 3A).
173   Endogenous FMR1 is also present as a network in cells (Fig. S4F, S4G). In HeLa cells, the
174   FXR1 and FMR1 networks partially overlap (Fig. S4G-I). Similar to FXR1, the folded domains in
175   the N-terminus were sufficient for formation of spherical granules and addition of the RG domain
176   of the IDR connected the granules and induced network formation (Fig. S4J, S4K). FMR1 also
177   required intact CC domains for network assembly and stable RNA binding (Fig. 3B, 3C).

178   Epigenetic silencing of *FMR1* causes FXS[13]. In a few patients, however, single FMR1 point
179   mutations in the KH1 (G266E) or KH2 (I304N) RNA-binding domains cause severe FXS disease
180   symptoms[42,43]. We modeled these mutations in FMR1 and FXR1 and observed that both point

181 mutations disrupted network assembly and reduced mRNA binding of FMR1 and FXR1 (Fig.
182 3B-E, S4C, S4L, Video S6 and S10)[42-44]. These results show that FMR1 also forms an mRNP
183 network and that RNA binding is required for network assembly, suggesting that FXR1 and
184 FMR1 need to be assembled into their respective networks to be functional.

185

186 **Single point mutations prevent assembly of the endogenous FXR1 network**

187 To study the effects of network disruption of endogenous FXR1, we used base editing to
188 introduce a single CC-breaking point mutation into endogenous *FXR1* in A549 cells. As only
189 CC1 was amenable to base editing, we generated cells with an N202S mutation in FXR1 (Fig.
190 3F). This mutation disrupted the endogenous FXR1 network and reduced mRNA binding in
191 oligo(dT) pulldown experiments (Fig. 3F-I).

192 As the CC mutation disrupts mRNA binding and FXR1 dimerization, we tested whether
193 disruption of mRNA binding alone is sufficient to prevent FXR1 network assembly. Using prime
194 editing, we generated the FXS patient-derived mutation G266E in the KH1 domain of
195 endogenous *FXR1* in A549 cells (Fig. 3J). Endogenous FXR1-G266E has a strongly reduced
196 mRNA binding ability in oligo(dT) pulldown experiments (Fig. 3K, 3L). These results reveal that
197 disruption of mRNA binding of FXR1 is sufficient to disrupt FXR1 network assembly (Fig. 3M),
198 indicating that mRNA is the underlying scaffold of the FXR1 network.

199

200 **Exceptionally long mRNAs bound to FXR1 dimers serve as scaffold of the FXR1 network**

201 To start to address a potential function of the FXR1 network, we used individual-nucleotide
202 resolution UV-cross-linking and immunoprecipitation (iCLIP) to identify FXR1-bound mRNAs in
203 HeLa cells. To identify FXR1 network-dependent mRNAs, we depleted endogenous FXR1 and
204 replaced it with either GFP-tagged WT or the assembly-deficient CC2-mutant FXR1 (Fig. S5A,
205 S5B)[45]. We observed that, within mRNAs, FXR1 binds nearly exclusively to 3′UTRs or coding
206 sequences (Fig. S5C, 50.6% and 46.8% of binding sites, respectively). We regard 2,327
207 mRNAs as FXR1 targets and validated 19/20 using RNA-IP followed by qRT-PCR (Fig. S5D,
208 S5E).

209 We define network-dependent mRNAs as FXR1 targets whose binding is reduced by at least
210 two-fold, when comparing the binding pattern of WT and assembly-deficient FXR1.
211 Approximately half ($N = 1223$) of the FXR1 targets are network-dependent, whereas RNA-
212 binding of the other half of FXR1 targets ($N = 1104$, 47%) was not affected by the assembly-
213 deficient FXR1 mutant, and therefore are called network-independent targets (Fig. S5F, Table
214 S1).

215 Comparison of network-dependent and -independent mRNAs revealed that the former have
216 nearly twice as many FXR1 binding sites and are significantly longer, thus representing
217 exceptionally long mRNAs with a median length of ~6,000 nucleotides (Fig. 4A, 4B). They are
218 also characterized by the highest AU-content and the longest 3′UTRs (Fig. 4C, S5G). Taken
219 together, these results suggest a model whereby FXR1 dimers bind to the longest mRNAs
220 expressed in cells, which allows them to be packaged into the FXR1 network, where they form
221 the underlying mRNA-FXR1 dimer scaffold. Therefore, we call the network-dependent targets
222 scaffold mRNAs of the FXR1 network. As network-independent mRNAs were only detected
223 after cross-linking, these results suggest that they are not packaged into the network but may
224 only associate with it. This model is consistent with the oligo(dT) pull-down experiments (see
225 Fig. 2E), which were performed without cross-linking and only detected mRNAs strongly bound
226 to FXR1 dimers (Fig. 2E, 3E, 3H, 3L).

227

The FXR1 network provides a signaling scaffold for RhoA-induced actomyosin reorganization

230 To obtain insights into the physiological role of the FXR1 network, gene ontology analysis was
231 performed to identify enriched pathways among the FXR1 scaffold mRNAs[46]. We observed a
232 significant enrichment of various signaling pathway components, including kinases, GDP-
233 binding proteins, and regulation of the actin cytoskeleton (Fig. 4D).

234 A closer look into the FXR1 targets involved in actin cytoskeleton dynamics revealed that nearly
235 all components of the RhoA-activated actomyosin remodeling pathway are encoded by FXR1-
236 bound mRNAs (Fig. 4E, boxes with black outline, Table S1). Dynamic regulation of the
237 actomyosin cytoskeleton is fundamental to basically all cell types and controls cell shape,
238 adhesion, migration, and synaptic function[47-49]. The components of the RhoA signaling pathway
239 are ubiquitously expressed and the pathway is induced by diverse extracellular signals, such as
240 lysophosphatidic acid (LPA) or thrombin, which activate G protein-coupled receptors, thus
241 activating the RhoA GTPase[23,50]. Active RhoA binds and activates the Rho-associated kinase
242 ROCK, the central regulator of actomyosin remodeling[51]. The crucial regulatory event for
243 actomyosin remodeling is the phosphorylation of the regulatory light chains (RLC) of non-
244 muscle myosin II (NM II). NM II is a hexamer that consists of two myosin heavy chains, two
245 essential light chains and two RLCs. The RLCs are directly phosphorylated by ROCK[52]. RLC
246 phosphorylation can also be increased through inhibition of phosphatase 1, which is mediated
247 by ROCK-dependent phosphorylation of MYPT1, the regulatory subunit of phosphatase 1 (Fig.
248 4E). Importantly, RLC phosphorylation induces actin bundling and contraction of actin fibers,
249 which can be read out as stress fiber formation.

250 To determine whether FXR1 is required for stress fiber formation, we treated A549 cells with
251 thrombin or LPA and stained them for filamentous actin (F-actin) (Fig. 4F). RhoA stimulation-
252 induced stress fibers were generated in cells that express control shRNAs, but their formation
253 was strongly reduced in cells treated with shRNAs against *GNA13*, *ROCK2,* or *FXR1* (Fig. 4F,
254 4G, S6A-E). Since ROCK2 knockdown was sufficient to disrupt stress fiber formation and
255 *ROCK2* mRNA was a validated FXR1 target (Fig. S5E), we focused on ROCK2 instead of
256 ROCK1 for the rest of the study. Regulation of stress fiber formation was specific to FXR1, as
257 FMR1 knockdown did not affect their formation (Fig. S6A-C). These results show that FXR1
258 protein is required for Rho A signaling-induced actomyosin remodeling. Importantly, the
259 network-disrupting point mutations in endogenous FXR1 (N202S or G266E) also prevented
260 stress fiber formation (Fig. 4H-K), demonstrating that not only the presence of FXR1 protein, but
261 FXR1 assembled into the FXR1 network, is essential for RhoA signaling-induced actomyosin
262 remodeling.

263 Actomyosin remodeling can positively or negatively affect cell migration[53-55]. We observed that
264 FXR1 knockdown or ROCK inhibition impaired migration of A549 cells (Fig. S6F). When testing
265 whether the FXR1 network is required for migration, we observed that migration in all single cell
266 clones with WT phenotype was strongly reduced (Fig. S6G), indicating that the generation of
267 single cell clones impairs the migration capacity of the cells, which confounded the investigation.

268

Phosphorylation of RLC by ROCK2 kinase is FXR1 network-dependent

270 How does the FXR1 network regulate actomyosin dynamics? As FXR1 was reported to regulate
271 translation[21], we hypothesized that protein levels in the RhoA signaling pathway are regulated
272 by FXR1. To identify FXR1-dependent protein abundance changes, we performed Tandem
273 Mass Tag quantitative proteomics analysis in control and FXR1 knockdown cells. Surprisingly,

274 among 7,067 expressed proteins, only six significantly changed expression in the absence of
275 FXR1, and none of them were components of the RhoA signaling pathway (Fig. 5A, Table S2).
276 Moreover, immunoblot analysis on the RhoA pathway components in unstimulated and
277 stimulated A549 cells, in the presence or absence of FXR1, did not detect FXR1-dependent
278 abundance changes of ROCK2, MYPT1, and the NM II subunits NM IIA and RLC (encoded by
279 MYH9 and MYL9) (Fig. S6H-J). These results indicated that FXR1 does not widely affect protein
280 abundance in the investigated cell types and does not control protein levels of the RhoA
281 signaling pathway.

282 To identify the molecular mechanism by which the FXR1 network impacts the signaling pathway
283 that controls actomyosin remodeling, we examined the pathway in greater detail. As FXR1
284 knockdown did not reduce the amount of active RhoA obtained through GPCR stimulation (Fig.
285 S6K), we concluded that the RhoA pathway upstream of ROCK is unaffected by FXR1
286 deficiency. We then discovered that RhoA signaling-induced RLC phosphorylation was FXR1
287 dependent (Fig. 5B, 5C). Importantly, RLC phosphorylation was impaired not only in cells with
288 knockdown of FXR1, but also impaired in cells with network-disrupting mutations (N202S or
289 G266E) of endogenous FXR1 (Fig. 5D-G). These data indicate that the FXR1 network is
290 essential for RhoA-signaling induced phosphorylation of NM II.

291

The FXR1 network provides proximity between the ROCK2 kinase and its substrate RLC

293 Phosphorylation of RLC requires an active ROCK2 kinase and spatial proximity between kinase
294 and substrate[51,56]. As phosphorylation of the ROCK2 substrate MYPT1 was FXR1-independent,
295 we concluded that ROCK2 activation does not rely on FXR1 (Fig. S6I, S6J). To determine
296 whether FXR1 acts as a scaffold for ROCK2 kinase and its substrate RLC, we performed a
297 Proximity Ligation Assay (PLA) in cells expressing control or FXR1-targeting shRNAs. PLA
298 allows the in-situ detection of protein:protein interactions whose distance is less than 40 nm
299 (Fig. 5H)[57]. After thrombin stimulation, the ROCK2 kinase is in proximity with both its substrates
300 MYPT1 and RLC in control cells, whereas in FXR1 knockdown cells, the proximity between
301 ROCK2 and RLC is strongly reduced (Fig. 5I, 5J, S6L).

302 Taken together, these results show that FXR1 is essential for RhoA signaling-induced
303 actomyosin remodeling, where the crucial signaling step is an FXR1 network-dependent event
304 that establishes spatial proximity between kinase and substrate. As FXR1 has a large number of
305 protein:protein interaction domains (Fig. 2A), we hypothesized that the FXR1 network may
306 therefore act as signaling hub.

307

Network-dependent protein interactors have similar protein domains as FXR1

309 To identify network-dependent protein:protein interactors of FXR1, we performed GFP co-
310 immunoprecipitation (co-IP) and SILAC proteomics analysis using GFP-FXR1 WT and
311 assembly-deficient CC2 mutant, expressed in cells depleted of endogenous FXR1 (Fig. 6A,
312 S7A). We identified several proteins, including FXR2, FMR1, UBAP2L, TOP3B, TDRD3,
313 PRRC2C, PRRC2A, and AP2A1, that interacted significantly better with WT FXR1 compared
314 with CC2 mutant FXR1 (Fig. 6A, Table S3). To validate these results, we performed co-IP in the
315 presence or absence of RNase A, followed by immunoblot analysis. This approach validated
316 10/10 candidates (Fig. 6B, 6C). We observed that most of these protein:protein interactions are
317 RNA-dependent, which supports their FXR1 network dependence (Fig. 6B, 6C).

318 When analyzing the protein domains of the network dependent FXR1 interactors, we made the
319 surprising observation that the interactors contain the same kinds of protein domains as FXR1

320 (Fig. 6D). FXR1 contains CC, Tudor, and RGG domains and these domains were significantly
321 enriched among the top 20% of network-dependent FXR1 binding partners (Fig. 6E, Tables S1
322 and S3). Moreover, FXR1 mRNA targets were significantly enriched among the FXR1 protein
323 interactors (Table S3). As CC, Tudor and RGG domains can perform homo- and
324 heterodimerization[28,30,37-39], these data suggest that proteins may use these domains to become
325 recruited into the FXR1 network, thus acting as protein clients of the network. We hypothesized
326 that signaling proteins containing these domains become recruited into the FXR1 network and
327 use the network to achieve spatial proximity.

328

329 **The CC domain of ROCK2 binds to FXR1**

330 FXR1 network-dependent proximity occurs between ROCK2 and NM II (Fig. 5H-J). Both
331 ROCK2 and NM II contain large CC domains (Fig. 7A). To determine whether the CC domains
332 of ROCK2 interact with FXR1, we performed co-IP of GFP-tagged ROCK2 truncation constructs
333 (Fig. 7B). We observed that the C-terminal half of ROCK2 strongly interacts with FXR1 (Fig.
334 S7B, S7C). As the interaction requires the presence of the CC2 domain of ROCK2, the results
335 indicate that this CC domain is necessary for FXR1 binding (Fig. 7C). This finding is consistent
336 with a model whereby proteins that contain binding sites for FXR1 are recruited into the FXR1
337 network (Fig. S7D).

338

339 **CC, Tudor or RGG domains are sufficient for binding to FXR1**

340 Finally, we determined whether the presence of a single proposed domain (CC, Tudor, or RGG)
341 was sufficient for binding to FXR1. GFP-tagged GAPDH, an enzyme that does not interact with
342 FXR1, was fused to either the CC2 domain of ROCK2, the RGG domain of TOP3B, the Tudor
343 domain of TDRD3, the R-rich domain of TDRD3, or both domains (Fig. 7D, S7E). Co-IP
344 demonstrated that all GAPDH-fusion proteins interacted with endogenous FXR1, whereas
345 GAPDH alone did not (Fig. 7E, 7F). Whereas the presence of a single FXR1 protein interaction
346 domain was sufficient for FXR1 binding, the binding was weak for two of the four tested
347 domains. Importantly, the presence of two interaction domains, such as a Tudor and an R-rich
348 domain, showed a cooperative effect for FXR1 binding and increased the affinity by ~20-fold
349 (Fig. 7E, 7F).

350

351 **Discussion**

352 Here, we report the discovery of the FXR1 network—a large cytoplasmic mRNP network that
353 acts as a multivalent signaling platform. The FXR1 network is present throughout the cytoplasm
354 of all cells so far investigated. In addition to spherical condensates like P bodies and stress
355 granules, our work shows that the cytoplasm is further compartmentalized by several network-
356 like condensates, including TIS granules and the FXR1 network[5-7].

357

358 **Regulation of proximity of signaling proteins by the FXR1 network**

359 The underlying scaffold of the FXR1 network are exceptionally long mRNAs that are bound and
360 packaged by FXR1 dimers (Fig. 7G). Only a minority of FXR1 stably binds to mRNA and is part
361 of the underlying scaffold. As FXR1 is nearly entirely present within high-molecular-weight
362 complexes, most FXR1 molecules act as clients and are recruited into the network using
363 protein:protein interactions through multiple CC, Tudor, and RGG domains, which are known for
364 their homo- and heterodimerization capacities[28,30,37-39]. Homodimerization recruits FXR1

365 molecules into the network, whereas heterodimerization recruits other proteins, such as
366 signaling factors. The high concentration of FXR1 molecules in the network generates a high
367 concentration of binding sites for CC, Tudor, and RGG domains and allows multivalent binding
368 of recruited clients, including signaling proteins, which brings these molecules into proximity with
369 each other (Fig. 7G).

370 Point mutations in the KH domains or in the CC domains prevent RNA binding of FXR1 and
371 prevent formation of the network scaffold, which results in diffusive FXR1 protein. Network
372 disruption lowers the local FXR1 concentration, thus preventing transient trapping of signaling
373 molecules and network-dependent spatial proximity, which impairs enzyme-substrate
374 interactions and prevents productive signal transduction (Fig. 7G). Thus, the FXR1 network
375 brings proteins containing certain CC, Tudor, or RGG domains into proximity to promote key
376 signaling pathways, as we demonstrated for actomyosin remodeling. As many other signaling
377 proteins also contain these domains[29], it is likely that additional signaling pathways use the
378 FXR1 network as scaffold.

379

380 The FXR1 network is essential for actomyosin remodeling and is disrupted by disease
381 mutations

382 Single point mutations (G266E or I304N) in FXR1 disrupt the FXR1 network. The mutations
383 were detected in the FXR1 homolog FMR1, where they cause FXS[13,27,42]. FXS is the most
384 common inherited cause of intellectual disability and is one of the most common inherited
385 causes of ASD[20]. Variants in the *FXR1* gene are also strongly associated with increased risk for
386 ASD and schizophrenia[14-17]. Deletion of FXR1 in mouse interneurons reduces their excitability
387 and causes schizophrenia-like symptoms[20], suggesting a role for FXR1 in neuronal functions.

388 One of the physiological phenotypes caused by FXR1 network disruption is impaired
389 actomyosin cytoskeleton remodeling, a process that occurs in nearly all cell types[47-49]. In non-
390 neuronal cells, it is essential for the regulation of cell shape, adhesion, migration, and tissue
391 architecture, whereas in neuronal cells it also controls dendritic spine morphology and synaptic
392 function[47-49]. Alterations in spine morphology are associated with neuronal dysfunction and can
393 lead to cognitive and behavioral problems[58,59]. Therefore, we suggest that FXR1 network
394 disruption, which impairs actomyosin dynamics, could be one of the underlying causes of
395 abnormal dendritic spine morphology and synaptic function in patients with FXS.

396

397 Do FXR1 and FMR1 have overlapping functions?

398 FMR1 is also present as mRNP network in the cytoplasm. Moreover, FXR family members bind
399 to each other and are incorporated into each other's networks[26]. To address whether FXR1 and
400 FMR1 have overlapping functions, we tested the requirement of FMR1 for stress fiber formation
401 and found that in A549 cells, only FXR1 was necessary for RhoA signaling-induced stress fiber
402 formation. We suspect that the functions of FXR family proteins strongly depend on their
403 expression levels, because dosage reduction of assembly-competent WT FXR1 in the samples
404 with heterozygous FXR1 mutations was sufficient to impair stress fiber formation. The mRNA
405 expression pattern of the three FXR family homologs shows that FXR1 is expressed
406 ubiquitously at very high levels, whereas FMR1 and FXR2 are mostly expressed in the brain,
407 suggesting that in non-neuronal cell types FXR1's function may be dominant.

408

409 Molecular principles of the mRNA scaffold

410 FXR1 binds and packages the longest ~1200 mRNAs expressed in cells, which results in the
411 formation of an mRNP network. Most mRNAs are packaged into individual mRNPs by the exon-
412 junction complex, which binds to exon-intron junctions in coding sequences[60]. The FXR1-bound
413 mRNAs have very long 3′UTRs, which lack exon-intron junctions, suggesting that FXR1 may
414 have a packaging function for these mRNAs. This idea is supported by the ubiquitous and high
415 expression of FXR1[23], which suggests that the role of FXR1 is required in all cells. Moreover,
416 the intrinsic binding affinity of FXR1 to RNA seems very weak[61]. We speculate that the weak
417 RNA binding affinity of FXR1 is responsible for the selection of long 3′UTRs as they provide the
418 largest number of potential binding sites.

419 In addition to the FXR1 network, also TIS granules have a network-like structure, generated
420 through RNA-RNA interactions[10]. We showed that FXR1 network formation requires RNA
421 binding of the RG motif in the FXR1 IDR. RG motifs bind to RNA and remodel RNA-RNA
422 interactions during RNA annealing reactions[36,62,63], suggesting that RG motifs play crucial roles
423 in the formation of network-like condensates.

424

Molecular principles of FXR1 network-dependent proximity of clients

426 We showed how a large mRNP network serves as signaling scaffold for proteins that do not
427 contain RNA-binding domains. Specificity of the FXR1 network-based signaling platform is
428 provided by CC, Tudor, and RGG domains. In addition to Tudor-Tudor or RGG-RGG
429 interactions, Tudor-RGG interactions are also possible, as Tudor domains bind to methylated
430 arginines, usually in the context of RG/RGG domains[25,29]. RG/RGG domains seem to be the
431 most versatile domains in this system as they can bind to RNA and protein[25,28-30]. Although RGG
432 domains are often found in nuclear and RNA-binding proteins, in the cytoplasm, they are
433 observed in structural and regulatory factors, including intermediate filaments, cytoskeleton-
434 binding proteins, and kinases[29]. Therefore, we propose that cytoskeletal processes that need to
435 be coordinated within the entire cytoplasm may take advantage of the FXR1 network because it
436 provides a scaffold to promote signaling events throughout the cytoplasm.

437 In addition to proteins or lipid membranes acting as signaling scaffolds[64,65], we uncovered
438 another type of signaling scaffold in the form of an mRNP network. Its underlying scaffold is
439 generated by FXR1-bound mRNAs, revealing that mRNAs perform structural roles in the
440 cytoplasm. We show that the function of mRNAs and RNA-binding proteins can go beyond the
441 regulation of mRNA-based processes[66]. So far, RNA-binding proteins are generally considered
442 to regulate mRNA stability, translation, or localization. However, we demonstrate that they can
443 affect signaling pathways and cytoskeleton processes, thus broadening the impact of mRNA
444 and RNA-binding proteins on cellular processes.

445

Limitations of the study

447 This study was performed with cell lines grown in culture. Therefore, the physiological functions
448 of the FXR1 network in living animals are currently unknown. We documented the requirement
449 of the FXR1 network for one step of an important signaling pathway. However, the FXR1 mRNA
450 targets are enriched for many other signaling factors, including ubiquitin ligases, but we
451 currently do not know the scope of signaling reactions that are FXR1 network dependent. To
452 identify FXR1 network-dependent interactors, we used affinity purification-mass spectrometry,
453 but this method only captures interacting proteins with relatively high affinity or abundance.
454 During cell lysis, protein concentration is strongly reduced, potentially leading to the loss of low
455 affinity interactors. This is relevant for the study of condensates, where protein concentration is
456 key to condensate formation. Labeling the neighboring molecules before cell lysis through

457 proximity ligation may provide more FXR1 network-enriched signaling proteins to allow
458 identification of additional FXR1 network-dependent biochemical reactions.

459
460
461 **Acknowledgements**

469

470 **Author contribution**

471 X.C. performed all experiments, except the FXR1 iCLIP experiment, which was performed and
472 analyzed by U.J. and J.U. M.M.F provided the gene features. X.C. and C.M. conceived the
473 project, designed the experiments, and wrote the manuscript with input from all authors. We
474 thank members of the Mayr lab, and Nancy Bonini (U Penn) for critical reading of the
475 manuscript and for helpful discussions.

476

477 **Declaration of Interests**

478 Christine Mayr is a member of the Cell Advisory Board.

479 The authors declare no other competing interests.

480

481

482 **Figure Legends**

483 **Figure 1. FXR1 assembles with its bound mRNAs into a cytoplasmic mRNP network.**

484 **A.** Immunofluorescence staining of endogenous FXR1 protein in HeLa cells. The dotted line
485 indicates the nucleus. Right panel is a zoomed-in image of the region in the yellow box. All cells
486 contain the network, and a representative confocal image is shown. All scale bars in Figure 1
487 are 5 μm.

488 **B.** Live cell confocal imaging of HEK293T cells with endogenous monomeric NG-tagged FXR1
489 protein. All cells contain the network and a representative image is shown.

490 **C.** Size exclusion chromatography of cells from (**B**), immunoblotted for FXR1. CLUH was used
491 as loading control. mNG-FXR1 and FXR1 have the same elution pattern.

492 **D.** IUpred2A score of human FXR1. A score greater than 0.5 indicates an IDR. Schematics of
493 GFP-fusion constructs. The numbers denote amino acids.

494 **E.** Live cell confocal imaging of HeLa cells transfected with the FXR1 constructs from (**D**) after
495 knockdown of endogenous FXR1. The GFP fluorescence pattern shown for each construct was
496 observed in all cells expressing the respective FXR1 constructs. Representative images are
497 shown. See Fig. S4C for quantification.

498 **F.** Confocal imaging of HeLa cells transfected with GFP-FXR1-N2 after digitonin
499 permeabilization in the presence or absence of RNase A treatment for 30 minutes.
500 Representative images from at least three independent experiments are shown, where 21 cells
501 were examined.

502 **G.** FRAP analysis of GFP-FXR1-FL, -N1, and -N2 expressed in HeLa cells. Shown is a
503 normalized FRAP curve as mean ± std from at least 11 cells each. MF, mobile fraction. See
504 Videos S7-9 for representative fluorescence recovery. Mann-Whitney test, N1 vs. FL, ***, $P<10^{-21}$;
505 N2 vs. FL, ***, $P<10^{-165}$.

506

507

Figure 2. FXR1 dimerization through the CC domains promotes mRNA binding and nucleates the FXR1 network.

510 **A.** Amino acid boundaries of FXR1 protein domains. Domains capable of binding to RNA or
511 protein are indicated.

512 **B.** Schematic of FXR1 CC mutant constructs and their resulting FXR1 network assembly states.
513 Red star symbols represent single point mutations. CC1mut is N202P, CC2mut is V361P. See
514 Fig. S4A-E for details.

515 **C.** Live cell confocal imaging of HeLa cells transfected with GFP-FXR1 constructs from (**B**) after
516 knockdown of endogenous FXR1, shown as in Fig. 1**A**. Representative images from at least
517 three independent experiments are shown where 38 cells were examined. See Fig. S4C for
518 quantification. Scale bar, 5 µm.

519 **D.** GFP co-IP of endogenous FXR1 after ectopic expression of GFP-FXR1-WT or GFP-FXR1-
520 CC2mut in HeLa cells. Actin is shown as loading control. 1% of input was loaded.

521 **E.** Oligo(dT) pulldown, performed without cross-linking, of mRNA-bound FXR1 in
522 FXR1/FXR2/FMR1 triple KO U2OS cells after ectopic expression of GFP or GFP-FXR1
523 constructs from (**B**). The endogenously expressed RNA-binding protein HuR was used as
524 positive and loading control for oligo(dT)-bound proteins. 2.5% and 5% of input were loaded in
525 the left and right panels, respectively.

526

527

Figure 3. The FXS mutations I304N and G266E disrupt the FMR1 and FXR1 networks.

529 **A.** Amino acid boundaries of FMR1 protein domains and schematics of FMR1 constructs.

530 **B.** Live cell confocal imaging of HeLa cells transfected with GFP-FMR1 constructs from (**A**),
531 shown as in Fig. 1**A**. All cells with WT-FMR1 contain the network and most cells with mutant
532 FMR1 show network disruption (see Fig. S4C for quantification). Representative images are
533 shown. Scale bar, 5 µm.

534 **C.** Oligo(dT) pulldown, performed without cross-linking, of mRNA-bound FMR1 in
535 FXR1/FXR2/FMR1 triple KO U2OS cells after ectopic expression of GFP or GFP-FMR1
536 constructs from (**A**). The endogenous RNA-binding protein HuR was used as positive and
537 loading control for oligo(dT)-bound proteins. 1% of input was loaded.

538 **D.** Live cell confocal imaging of HeLa cells transfected with GFP-FXR1-WT or FXS mutant
539 constructs after knockdown of endogenous FXR1, shown as in (**B**). The FXS mutations G266E

540 and I304N are located at the same amino acid positions in FXR1 and FMR1. The network is
541 disrupted in all cells (see Fig. S4C for quantification). Representative images are shown.

542 **E.** As in (**C**), but oligo(dT) pulldown was performed after ectopic expression of GFP-FXR1-WT, -
543 G266E, or -I304N.

544 **F**. Sanger sequencing results of heterozygous and homozygous N202S CC1-disrupting point
545 mutations in endogenous *FXR1* in A549 clonal cells generated using base editing.

546 **G.** Oligo(dT) pulldown of mRNA-bound FXR1 in A549 clonal cells from (**F**). Endogenous HuR
547 was used as positive and loading control for oligo(dT)-bound proteins. 1% of input was loaded.

548 **H**. Quantification of FXR1-bound mRNAs from (**G**) shown as mean ± std obtained from three
549 independent experiments. One-way ANOVA, *** $P<0.001$.

550 **I.** Live cell confocal imaging of A549 clonal cells from (**F**) after knockin of monomeric GFP into
551 the endogenous *FXR1* locus. Scale bar, 5 µm.

552 **J**. Sanger sequencing results of heterozygous KH1 domain point mutation G266E in
553 endogenous *FXR1* in A549 clonal cells generated using prime editing.

554 **K.** Oligo(dT) pulldown of mRNA-bound FXR1 in A549 clonal cells from (**J**). Endogenous HuR
555 was used as positive and loading control for oligo(dT)-bound proteins. 0.2% of input was
556 loaded.

557 **L**. Quantification of FXR1-bound mRNAs from (**K**) shown as mean ± std obtained from three
558 independent experiments. One-way ANOVA, *, $P<0.05$, **, $P<0.01$.

559 **M**. Schematic summarizing the results from (**F**) to (**L**).

560

561

562 **Figure 4. The FXR1 network is required for RhoA signaling-induced actomyosin**
563 **reorganization.**

564 **A.** All mRNAs expressed in HeLa cells are grouped based on their FXR1 binding pattern.
565 mRNAs not bound by FXR1 (*N*=6574), bound by FXR1 but network-independent (*N*=1104),
566 bound by FXR1 and network-dependent (*N*=1223). Boxes represent median, 25th and 75th
567 percentiles, error bars represent 5-95% confidence intervals. Mann-Whitney test, ***, $P<10^{-53}$.

568 **B.** As in (**A**), but mRNA length is shown. Mann-Whitney test, ***, $P<10^{-14}$.

569 **C.** As in (**A**), but AU-content of mRNAs is shown. Mann-Whitney test, ***, $P<10^{-54}$.

570 **D.** Gene ontology analysis for FXR1 network-dependent mRNA targets. Shown are the top
571 functional gene classes and their Bonferroni-corrected *P* values.

572 **E**. Schematic of RhoA signaling pathway-induced actomyosin remodeling. The critical signaling
573 event for actomyosin dynamics is RLC phosphorylation of NM II. Protein symbols with black
574 outlines are FXR1 mRNA targets. ELC, essential light chain. P, phosphorylated residue.

575 **F.** Phalloidin staining of filamentous actin in A549 cells expressing the indicated shRNAs after
576 serum starvation and stimulation with thrombin for 30 minutes. DAPI staining visualizes the
577 nucleus. Representative images are shown. Scale bar, 40 µm.

578 **G.** Quantification of the experiment in (**F**) shown as mean ± std obtained from at least three
579 independent experiments. For each experiment and each sample at least 150 cells were
580 counted, except for the *ROCK2* KD experiment, where 34 cells were counted. One-way
581 ANOVA, ****, $P<0.0001$.

582 **H**. As in (**F**), but A549 clonal cells with heterozygous N202S mutations in endogenous *FXR1*
583 were used. Shown are representative images.

584 **I.** Quantification of the experiment in (**H**) shown as mean ± std obtained from at least three
585 independent experiments. For each experiment and each sample at least 28 cells were
586 counted. One-way ANOVA, ****, *P*<0.0001.

587 **J**. As in (**F**), but A549 clonal cells with heterozygous G266E mutations in endogenous *FXR1*
588 were used. Shown are representative images.

589 **K.** Quantification of the experiment in (**J**) shown as mean ± std obtained from three independent
590 experiments. For each experiment and each sample, at least 70 cells were counted. One-way
591 ANOVA, ****, *P*<0.0001.

592

593

594 **Figure 5. Phosphorylation of RLC by ROCK2 kinase is FXR1 network dependent.**

595 **A.** Tandem Mass Tag quantitative proteomics analysis of HeLa cells after control or *FXR1* KD.
596 Proteins whose abundance was significantly affected by *FXR1* KD are colored red (*N*=6),
597 whereas proteins not significantly affected are colored in blue (*N*=7061).

598 **B.** Western blot of the indicated endogenous proteins in A549 cells grown in the indicated
599 conditions. Ctrl, expressing control shRNA, KD, expressing FXR1 shRNA1. TCP1 was used as
600 loading control.

601 **C.** Quantification of phospho-RLC level from (**B**) shown as mean ± std obtained from at least
602 three independent experiments. One-way ANOVA, **, *P*< 0.01. n.s., not significant.

603 **D.** Western blot of the indicated proteins in serum-starved and thrombin-stimulated parental
604 A549 and clonal cell lines containing WT FXR1 or a heterozygous N202S mutation in
605 endogenous *FXR1*. α-Tubulin was used as loading control.

606 **E.** Quantification of phospho-RLC level from (**D**) shown as mean ± std obtained from three
607 clonal cell lines each. One-way ANOVA, **, *P*<0.01.

608 **F.** Western blot of the indicated proteins in serum-starved and thrombin-stimulated parental
609 A549 and clonal cell lines containing WT FXR1 or a heterozygous G266E mutation in
610 endogenous *FXR1*. α-Tubulin was used as loading control.

611 **G.** Quantification of phospho-RLC level from (**F**) shown as mean ± std obtained from two clonal
612 cell lines each.

613 **H**. Schematic of the proximity ligation assay (PLA), which generates a positive signal if the
614 distance between two endogenous proteins is smaller than 40 nm.

615 **I.** PLA performed in serum-starved thrombin-stimulated A549 cells, indicating that FXR1 is
616 required for proximity between ROCK2 and RLC, but not for proximity between ROCK2 and
617 MYPT1. As negative control, the RLC antibody alone was used. DAPI staining visualizes the
618 nucleus. Representative images are shown. Scale bar, 20 μm.

619 **J.** Quantification of the experiment in (**I**), shown as mean ± std of three independent
620 experiments. For each experiment and each sample at least 39 cells were counted. One-way
621 ANOVA, ****, *P*<0.0001.

622

623 **Figure 6. FXR1 network-dependent protein interactors contain CC, Tudor, and RGG**
624 **domains.**

625 **A.** SILAC mass spectrometry analysis of HeLa cells. Shown is log2 fold change (FC) of protein
626 counts of CC2mut/WT samples. Reduced interaction in CC2 mutant samples indicates that the
627 interaction with FXR1 is network dependent. The top network dependent FXR1 interactors are
628 indicated. For full list, see Table S3.

629 **B.** Validation of the SILAC proteomics results using GFP co-IP of the indicated endogenous
630 proteins followed by western blot in the presence or absence of RNase A. GFP-FXR1
631 constructs were ectopically expressed in HeLa cells depleted of endogenous FXR1. 0.5% input
632 was loaded.

633 **C.** As in (**B**), but GFP co-IP of endogenous FXR1 by ectopically expressed interactors. The red
634 star symbol marks an unspecific band. 1% input was loaded.

635 **D.** Protein domains of the top FXR1 network-dependent interactors. Shown are CC, Tudor,
636 RG/RGG, and R-rich domains in color.

637 **E.** Fold enrichment of indicated protein domains in the 20% of proteins from (**A**) with the most
638 negative FC. Shown is the observed-over-expected frequency. Chi-square test, **, P=0.002, ***,
639 P<0.0001. Chi-square test for Tudor domains cannot be performed as the numbers are too
640 small. See Table S3.

641
642

643 **Figure 7. The presence of CC, Tudor, or RGG domains is sufficient for binding to FXR1.**

644 **A.** Protein domains of NM II (MYH9), RLC (MYL9), and ROCK2. Highlighted are CC and R-rich
645 domains.

646 **B.** Amino acid boundaries of ROCK2 protein domains and schematics of ROCK2 constructs.
647 The numbers indicate amino acids.

648 **C.** GFP co-IP, followed by western blot of endogenous FXR1 after ectopic expression of GFP-
649 ROCK2-C or GFP-ROCK2-C-ΔCC (from **B**) in HeLa cells. 1% input was loaded.

650 **D.** Schematic of GFP-GAPDH fusion constructs. The following domains were fused to GAPDH:
651 CC2 domain of ROCK2, RGG domain of TOP3B, Tudor domain of TDRD3, R-rich region of
652 TDRD3, and both the Tudor and R-rich regions of TDRD3. See Fig. S7E for their amino acid
653 sequences.

654 **E.** GFP co-IP, followed by western blot of endogenous FXR1 after ectopic expression of GFP-
655 GAPDH fusion constructs from (**D**) in HeLa cells. A representative experiment is shown.

656 **F.** Quantification of (**E**). Shown is FXR1 enrichment normalized to sample C2 (shown in
657 magenta) as mean ± std obtained from at least three independent experiments.

658 **G.** Model of the FXR1 network and its function as a scaffold for signaling reactions by
659 establishing spatial proximity between kinases and their substrates. P, phosphorylated residue.
660 See text for details.

661
662

663 **Supplementary Figure Legends**

664 **Figure S1. Gene and protein expression pattern of endogenous FXR1, related to Figure 1.**

665 **A.** The gene expression level of the FXR family proteins in various primary cells and tissues.
666 The red, blue, and light blue bars represent the mRNA expression levels of FXR1, FMR1, and
667 FXR2, respectively. The boxplots show the distribution of expression levels of all expressed
668 mRNAs in the indicated cell types, obtained from Han et al., (2020)[23]. Boxplots shown as in Fig.
669 4**A**.

670 **B.** Representative confocal images of immunofluorescence staining of endogenous FXR1
671 proteins in the indicated cell lines. U2OS, human osteosarcoma epithelial cell line; EBC-1,
672 HCC95, A549 are human lung carcinoma lines; MCF7, human breast cancer line; iPSC, human
673 induced pluripotent stem cells; HEK293T, human immortalized embryonic kidney cells.

674 **C.** Knockin strategy of mGFP or mNG into the N-terminus of endogenous *FXR1* using a
675 CRISPR-based approach.

676 **D.** Genotyping agarose gel with primer pairs shown in (**C**). The black star symbol marks an
677 unspecific PCR product.

678 **E.** Western blotting of FXR1 in parental and mNG knockin HEK293T cell lines.

679 **F.** Sanger sequencing results of the two PCR bands marked with magenta arrows in (**D**),
680 aligned to the mNG-FXR1 donor sequence. mNG, gRNA, and the introduced silent mutations
681 are highlighted with green, gray, and magenta boxes, respectively.

682 **G.** Live cell confocal imaging of endogenous FXR1 tagged with either mNG or mGFP in the
683 indicated cell lines. Representative images are shown. Scale bar, 10 µm.

684

685

686 **Figure S2. All main FXR1 isoforms can form the FXR1 network, related to Figure 1.**

687 **A.** Gene model depicting the exon structure of the two most common FXR1 splice isoforms in
688 non-muscle cells. The three shRNAs targeting FXR1 exons used in this study are highlighted as
689 sh3, sh5, and sh7. The epitope locations of the two antibodies used for immunofluorescence
690 staining shown in **(D)** are labeled.

691 **B.** The sequences of the C-terminal ends of human FXR1 isoforms a and b are shown.

692 **C.** Western blot of the indicated endogenous FXR1 proteins in HeLa cells stably expressing a
693 control (ctrl) shRNA (targeting luciferase) or shRNA3, shRNA5, and shRNA7 against FXR1.

694 **D.** Immunofluorescence staining of endogenous FXR1 protein in HeLa cells expressing the
695 control shRNA or the indicated FXR1-targeting shRNAs from (**A**). Isoform-specific antibodies, as
696 indicated in (**A**) were used. All cells contain the network and representative confocal images are
697 shown. Scale bar, 10 µm.

698 **E.** Western blot of FXR1 in HeLa cells expressing control shRNA or FXR1-targeting shRNA5
699 transfected with increasing amounts of shRNA5-resistant mGFP-FXR1 constructs. The boxed
700 condition was used for the rest of the study.

701 **F.** Live cell confocal imaging of HeLa cells transfected with the indicated FXR1 constructs.
702 Representative images are shown. See Fig. S4C for quantifications. Scale bar, 10 µm.

703

Figure S3. Formation of FXR1 granules and the FXR1 network requires RNA, related to Figure 1.

A. Human FXR1 IUpred2A score and schematics of the used constructs. The GXXG motif, required for RNA binding of FXR1 KH domains was mutated to GDDG. Red star symbols represent the positions of the introduced mutations.

B. Live cell confocal imaging of HeLa cells depleted of endogenous FXR1 and transfected with the indicated constructs. Representative images are shown as in Fig. 1**A**. See Fig. S4C for quantifications. Scale bar, 5 μm.

C. Live cell confocal imaging of HeLa cells depleted of endogenous FXR1 and transfected with the indicated constructs, shown as in Fig. 1**A**. All cells expressing FXR1-N2-5A generated spherical granules, whereas all cells expressing FXR1-N2-5K generated a network. Representative images are shown. See Fig. S4C for quantification. The 20 aa sequence that distinguishes FXR1-N2 from FXR1-N1 is shown and the arginine residues that are mutated are shown in bold. Scale bar, 5 μm.

D. Confocal imaging of HeLa cells transfected with GFP-FXR1-N2-5K after digitonin permeabilization in the presence or absence of RNase A treatment for 30 minutes. Representative images from at least three independent experiments are shown, where 40 cells were examined. Scale bar, 5 μm.

E. Frame one from the timelapse of GFP-FXR1-N1 analyzed in (**F**). The timelapse was recorded at an interval of 10 min, spanning 12 hours. Scale bar, 5 μm.

F. Quantification of the number and total area of the granules from the timelapse shown in (**E**). The fluctuations represent the granules entering and leaving the imaging plane.

G. Confocal imaging of HeLa cells transfected with GFP-FXR1-N1 or -N2 and their corresponding identified objects with connected pixels randomly colored. Scale bar, 5 μm.

H. Quantification of the object size shown as area (μm^2) from the images in (**G**). The data is presented as mean ± 95% CI. The number of objects identified is 522 and 87 for FXR1-N1 and -N2, respectively.

Figure S4. FMR1 assembles into an mRNP network using the same principles as identified for FXR1 and details on FXR1 CC mutants are shown, related to Figures 2 and 3.

A. Human FXR1 protein domain boundaries and amino acid (aa) sequence conservation score across metazoa. Also shown is the probability for CC formation according to NCOILs.

B. The three heptads in the predicted FXR1 CC2 domain and their neighboring aa are shown. Highly conserved residues from (**A**) are shown in red. The aa sequences of the FXR1 CC mutant constructs are shown in the bottom panel. The first heptad of CC2 was not targeted in any of the mutants because of its high conservation score.

C. Quantification of GFP-FXR1 or GFP-FMR1 signal distribution pattern of transfected fusion constructs used in this study. A total of at least 53 cells from three or more independent experiments were scored and shown as mean ± std. The GFP signal was scored as diffusive, mostly diffusive (as shown in Fig. S3B, FXR1-N1-KH1mut), assembled network, or spherical granule.

747 **D.** Western blot of ectopically expressed GFP-fusion proteins show comparable expression
748 levels across samples. GAPDH was used as loading control.

749 **E.** Size exclusion chromatography of cells shown in Fig. 2**C**. GFP-FXR1 fluorescence was
750 measured using a plate reader. Shown is mean ± std of three technical replicates obtained from
751 one fractionation experiment.

752 **F.** Immunofluorescence staining of endogenous FMR1 protein in HeLa cells expressing the
753 control shRNA and FMR1-targeting shRNAs. The antibody used for immunofluorescence
754 staining was clone 6B8 (BioLegend, Cat# 834601). Scale bar, 20 μm.

755 **G.** Representative deconvolved images of FMR1 (green) and FXR1 (magenta) double
756 immunofluorescence staining in HeLa cells. Scale bar, 5 μm.

757 **H.** Quantification of the fraction of colocalized volumes for FXR1 and FMR1 shown as mean ±
758 std from 21 high-resolution volumes of HeLa cells.

759 **I.** Pearson's correlation coefficient between FXR1 and FMR1 fluorescence signals shown as
760 mean ± std quantified from 21 high-resolution HeLa cells.

761 **J.** Human FMR1 IUpred2A score and schematics of the used FMR1 constructs.

762 **K.** Live cell confocal imaging of HeLa cells expressing the indicated GFP-FMR1 constructs.
763 Representative images are shown as in Fig. 1**A**. See Fig. S4C for quantifications. Scale bar, 5
764 μm.

765 **L.** FRAP analysis of GFP-FXR1-FL and -I304N expressed in HeLa cells. Shown is the
766 normalized FRAP curve as mean ± std from at least three cells each. MF: mobile fraction. See
767 Videos S7 and S10 for representative fluorescence recovery. Mann-Whitney test, ***, $P<10^{-57}$.

768

769

770 **Figure S5. Identification of FXR1 network assembly-dependent mRNA targets using iCLIP**
771 **and their validation, related to Figure 4.**

772 **A.** Western blot of endogenous and transfected FXR1 in HeLa cells expressing control shRNA
773 or FXR1-targeting shRNA5, transfected with shRNA5-resistant mGFP-FXR1-WT or mGFP-
774 FXR1-CC2mut. The samples in lanes 3 and 4 were crosslinked for the iCLIP experiment.
775 GAPDH was blotted as loading control.

776 **B.** Infrared scan showing crosslinked RNA and FXR1 complexes separated by SDS-PAGE. The
777 boxed regions were isolated for iCLIP sample preparation.

778 **C.** Pie chart showing the genomic distribution of unique iCLIP reads for FXR1 in CDS, 5′UTR,
779 and 3′UTRs.

780 **D.** Western blot of endogenous FXR1 with samples used in RNA immunoprecipitation (RIP)
781 without cross-linking. The FXR1 antibody (Novus Biologicals, NBP2-22246) predominantly
782 enriched FXR1 isoform a, whereas IgG did not enrich any FXR1 protein.

783 **E.** The number of FXR1 binding sites found in specified mRNAs is shown on the left. The right
784 part of the panel shows the fold change in RNA-immunoprecipitation (RIP) signal obtained
785 without cross-linking using FXR1 antibody compared to IgG, obtained by RT-qPCR analysis of
786 the indicated mRNAs in HeLa cells. Shown is mean ± std of three independent experiments.

787 **F.** Identification of network-dependent (N = 1223) and network-independent (N = 1104) FXR1
788 mRNA targets. Network-dependent targets were defined based on a reduction of at least two-

789   fold in FXR1 binding sites observed by iCLIP, when comparing WT and CC2mut FXR1.
790   Boxplots are shown as in Fig. 4**A**. Mann-Whitney test, ****, $P = 0$.

791   **G.** Distribution of 3′UTR length in the three groups from Fig. 4**A** and shown as in Fig. 4**A**. Mann-
792   Whitney test, ***, $P < 10^{-25}$.

793

794

795   **Figure S6. FXR1-dependent regulation of the RhoA signaling pathway, related to Figure 4**
796   **and Figure 5.**

797   **A**. Phalloidin staining of filamentous actin in A549 cells expressing the indicated shRNAs after
798   serum starvation and stimulation with LPA for 30 minutes. DAPI staining visualizes the nucleus.
799   Representative images are shown. Scale bar, 40 μm.

800   **B.** Quantification of the experiment in (**A**) shown as mean ± std obtained from at least three
801   independent experiments. For each experiment and each sample at least 92 cells were
802   counted. One-way ANOVA, **** $P < 0.0001$. n.s., not significant.

803   **C.** Western blot of the indicated endogenous proteins from A549 cells shows knockdown
804   efficiency of shRNAs targeting *FXR1* and *FMR1*. The knockdown was specific, as no cross-
805   effect on FXR family proteins was observed.

806   **D.** As in (**C**), but knockdown efficiency of shRNAs targeting *FXR1* and *GNA13* is shown.

807   **E.** As in (**C**), but knockdown efficiency of shRNAs targeting *FXR1* and *ROCK2* is shown.

808   **F.** Fraction of migrated A549 cells for the indicated samples is shown as mean ± std from at
809   least three independent experiments. One-way ANOVA, ****, $P<0.0001$, **, $P<0.01$, *, $P<0.05$,
810   n.s., not significant.

811   **G.** Fraction of migrated A549 cells (parental) and the derived single cell clones with the
812   indicated FXR1 genotypes. Shown and quantified as in (**F**). One-way ANOVA, ****, $P<0.0001$,
813   ***, $P<0.001$, *, $P<0.05$, n.s., not significant. The migration capacity of the single cell clones with
814   WT genotype is significantly different from the parental cells. The migration capacity of the
815   single cell clones with mutant FXR1 is significantly different from the WT clones.

816   **H.** Western blot of the indicated endogenous proteins of the RhoA signaling pathway in A549
817   cells, grown in steady-state conditions and expressing the indicated shRNAs. α-Tubulin was
818   used as loading control.

819   **I.** Western blot of the indicated endogenous proteins of the RhoA signaling pathway in A549
820   cells after serum starvation and stimulation with thrombin for 10 minutes and expressing the
821   indicated shRNAs. GAPDH was used as loading control.

822   **J**. As in (**I**), but for shown for additional shRNAs. RLC T19 phosphorylation requires the
823   presence of ROCK1, ROCK2, and FXR1, whereas FXR1 KD did not change MYPT1 T853
824   phosphorylation level.

825   **K**. Active RhoA (RhoA-GTP) pulldown assay was performed in A549 cells expressing the
826   indicated shRNAs, which were serum-starved and treated with LPA for 5 minutes. The level of
827   active RhoA after GPCR activation is FXR1-independent.

828   **L.** Validation of the indicated RLC and ROCK2 antibodies for PLA assay using
829   immunofluorescence staining in A549 cells expressing the indicated shRNAs. The dilution factor
830   used for each antibody is shown. Scale bar, 40 μm.

831

832 **Figure S7. Proteins with binding sites for FXR1 are recruited into the FXR1 network,**
833 **related to Figure 7.**

834 **A**. Coomassie staining of the gel used for SILAC proteomics prepared from HeLa cells. The
835 three boxed areas represent the three gel slices processed for mass spectrometry analysis.

836 **B**. Schematic of ROCK2 protein domains and GFP-ROCK2 constructs used.

837 **C**. GFP co-IP of endogenous FXR1 protein after ectopic expression of GFP or the GFP-tagged
838 ROCK2 constructs from (**B**) in HeLa cells. The two red star symbols mark a bleed-through
839 signal from the blot for ROCK2-C.

840 **D**. PLA performed in serum-starved and thrombin-stimulated A549 cells, indicating proximity
841 between FXR1 and RLC as well as FXR1 and MYPT1. As negative control, the FXR1 antibody
842 alone was used. DAPI staining visualizes the nucleus. Representative images of three
843 independent experiments are shown. Scale bar, 20 μm.

844 **E**. The amino acid sequences of the CC, Tudor, RGG, R-rich, and Tudor-R-rich domains fused
845 to the C-terminus of GAPDH are shown. This panel is related to Fig. 7**D-F**.

846

847

848 **STAR methods**

849 **RESOURCE AVAILABILITY**

850 *Lead contact*

851 Further information and requests for resources and reagents should be directed to and will be
852 fulfilled by the Lead contact, Christine Mayr (mayrc@mskcc.org).

853 *Materials availability*

854 • Plasmids generated in this study will be deposited to Addgene.

855 • Plasmids generated in this study not available at Addgene are available from the Lead
856 Contact.

857 • The FXR1 knockin cell lines and the FXR1-N202S and FXR1-G266E cell lines (together
858 with the control cell lines) generated in this study are available from the Lead Contact
859 with a completed Materials Transfer Agreement.

860 *Data and code availability*

861 • The data of the TMT mass spectrometry experiment were deposited in the MassIVE
862 repository (dataset identifier MSV000093384). The data of the SILAC mass
863 spectrometry experiment were deposited in the MassIVE repository (dataset identifier
864 MSV000093385).
865 • The HeLa RNA-seq sample and the FXR1 iCLIP data obtained from HeLa cells are
866 available at ArrayExpress (ArrayExpress accession E-MTAB-13545).
867 • Western blot data, raw imaging data and scripts for analysis will be deposited at
868 Mendeley.
869 • Any additional information required to reanalyze the data reported in this paper is
870 available from the lead contact upon request.

871

872 **EXPERIMENTAL MODEL AND STUDY PARTICIPANT DETAILS**

Cell lines

873
874 HeLa, a human cervical cancer cell line of female origin, was a gift from the Jonathan S.
875 Weissman lab (UCSF), provided by Calvin H. Jan. HEK293T, a human immortalized embryonic
876 kidney cell line of female origin, was purchased from ATCC. A549, a human lung cancer cell
877 line of male origin, and MCF7, a human breast cancer cell line, were gifts from the lab of Robert
878 Weinberg (Whitehead Institute). U2OS and U2OS FXR1, FXR2, and FMR1 triple knockout
879 (U2OS $\Delta\Delta$) cell lines were a gift from the lab of Shawn Lyons (Boston University)[24]. All above
880 cell lines were maintained at 37°C with 5% CO2 in Dulbecco's Modified Eagle Medium (DMEM)
881 containing 4,500 mg/L glucose, 10% heat inactivated fetal bovine serum, 100 U/ml penicillin and
882 100 µg/ml streptomycin. The human lung squamous cell lines EBC-1 and HCC95 were gifts
883 from the Anti-tumor Assessment Core Facility and the lab of Charles Rudin (MSKCC). They
884 were maintained in RPM1-1640 medium containing 10% heat-inactivated fetal bovine serum,
885 100 U/ml penicillin, and 100 µg/ml streptomycin. These cell lines have not been authenticated.
886 The human iPSC cell line 731.2B was obtained from the SKI Stem Cell Research Facility at
887 MSKCC[67]. The cells were maintained at 37°C with 5% CO2 in Stemflex medium (Thermo
888 Fisher, A3349401). All cell culture vessels were coated with hESC-qualified Matrigel (Fisher
889 Scientific, 354277). ROCK inhibitor (Y-27632, 10 µM, Stemcell Technologies, 73202) was
890 added to the medium when the cells were passaged with 0.5 mM EDTA.

891

Constructs

893 GFP fusion constructs. All GFP fusion constructs were generated in the pcDNA3.1-puro-EGFP
894 backbone as N-terminal fusion proteins with the original AUG omitted[7]. Monomeric (mGFP) was
895 generated through the A207K mutation in EGFP and used in all constructs.

896 Human FXR1 mRNA was PCR-amplified from a HEK293T cDNA library and inserted between
897 BsrGI and XhoI sites. The cDNA library was created with qScript cDNA SuperMix (Quantabio,
898 95048). A total of three isoforms were identified through Sanger sequencing: FXR1 isoform a
899 (NM_005087.3, 621 amino acids (aa)), isoform b (NM_001013438.3, 539 aa), and isoform X4
900 (XM_005247816.3). If not stated otherwise, FXR1 isoform a was used. The FMR1 isoform 1
901 (NM_002024.6, 632 aa) coding sequence was amplified from the plasmid #48690 (Addgene)
902 and inserted between BsrGI and EcoRV sites.

903 The GAPDH, TOP3B, and TDRD3 coding sequences were amplified from a HeLa cDNA library
904 and inserted into the pcDNA3.1-puro-EGFP vector. The N-terminus of ROCK2 (aa 1-940) was
905 amplified from the plasmid #70569 (Addgene) and cloned into the XhoI-linearized backbone
906 with Gibson assembly master mix (E2621L, NEB) to obtain pcDNA3.1-puro-mGFP-ROCK2-N.
907 The C-terminus of ROCK2 (aa 941-1388) was amplified from an A549 cDNA library and
908 inserted between BsrGI and EcoRV sites. These two libraries were created by SuperScript IV
909 VILO First-Strand Synthesis System (Invitrogen, 11756050). The N-terminus of ROCK2 was
910 also amplified, and Gibson assembled into BsrGI-linearized pcDNA3.1-puro-mGFP-ROCK2-C
911 to obtain the full-length ROCK2 construct. To generate pcDNA3.1-puro-mGFP-ROCK2-C-ΔCC,
912 a gene fragment derived from the sequence between the SpeI and BbvCI sites of ROCK2-C,
913 which lacked the sequence of the coiled-coil domain (aa 1046-1150) was synthesized
914 (Genewiz). The exact sequence is listed in Table S4. This fragment and the pcDNA3.1-puro-
915 ROCK2-C backbone were digested with SpeI and BbvCI. Since the backbone contained two
916 SpeI sites, two of the three resulting fragments were collected, and the 490 bp fragment
917 between SpeI and BbvCI was discarded. The other two fragments and the synthesized fragment
918 were then ligated.

919 The FXR1 and FMR1 N- and C-terminal truncation constructs as well as the CC mutants were
920 generated using PCR amplification of the desired coding sequence fragments and were
921 subcloned into the pcDNA3.1-puro-mGFP backbone. Single point mutations to prolines in
922 coiled-coil domains were introduced at the first amino acid of the predicted heptads. The exact
923 mutated residues are detailed in Fig. S4B and in the list of plasmids in the Key Resource Table.
924 Specific point mutations and coiled-coil swapping constructs were generated using pcDNA3.1-
925 puro-mGFP-FXR1a or FMR1 via site-directed mutagenesis with Pfu Ultra HF DNA polymerase
926 (Agilent). The second coiled-coil domain in FXR1 contains highly conserved residues in the first
927 predicted heptad (Fig. S4A). This heptad was not disturbed when generating the CC mutants.
928 The amino acid sequences of all FXR1 CC mutants are detailed in Fig. S4B.

929 GAPDH-fusion protein constructs were generated using Gibson assembly master mix with
930 EcoRI linearized pcDNA3.1-puro-EGFP-GAPDH and desired PCR-amplified fragments. The
931 amino acid sequences appended to GAPDH are shown in Fig. S7E. The pcDNA3.1-UBAP2L-
932 mGFP construct was a gift from Christopher Hammell (CSHL). All constructs were verified by
933 Sanger sequencing or whole plasmid sequencing. All oligos used for cloning are listed in Table
934 S4.

935 shRNA constructs. A control shRNA against luciferase (MISSION® shRNA SHC007) was
936 purchased. All other shRNAs were designed with the Broad Institute GPP web portal. DNA
937 oligonucleotides listed in Table S4 were used as shRNA precursors and inserted into a
938 backbone pLKO.1 vector (TRCN0000160812) between SgrAI and EcoRI sites. All vectors were
939 verified by Sanger sequencing with U6 primer.

940

Transfection

942 Besides CRISPR-based gene editing experiments, all transfections into HeLa and U2OS ΔΔΔ
943 cells were performed with Lipofectamine 2000 (Invitrogen, 11668019).

944 For testing the amount of pcDNA3.1-mGFP-FXR1a plasmid to transfect to mimic endogenous
945 FXR1 level, 500, 250, 125, and 62.5 ng of plasmid was mixed with 3 µl Lipofectamine,
946 respectively, and transfected into HeLa grown in 35 mm dishes. 250 ng was determined to be
947 the optimal amount. For all imaging-related experiments, 50 ng of FXR1 plasmid was mixed with
948 0.6 µl Lipofectamine to transfect one well of a 24-well plate. For other experiments, amounts
949 were scaled up according to the surface area of the dish. For pcDNA3.1-puro-mGFP-FMR1,
950 100 ng plasmid per well of a 24-well plate was transfected.

951 For GFP trap mediated co-immunoprecipitation, 6 µg DNA of TDRD3, UBAP2L, TOP3B,
952 GAPDH, or GAPDH-fusion constructs was transfected into HeLa cells seeded in 10 cm dishes
953 with 10 µl Lipofectamine 2000 in a total of 1 ml OPTI-MEM (Gibco, 31985062).

954

shRNA-mediated knockdown

956 Stable cell lines were generated for shRNA-mediated knockdown experiments. 2 µg pLKO.1
957 plasmid was co-transfected with 1.8 µg pCMV-dR8.2 and 0.2 µg pCMV-VSV-G with 7 µl
958 Lipofectamine 2000 into HEK293T cells seeded in 6-well plates one day ahead. The medium
959 was changed 6 hours after transfection. Viral particles were harvested 48 hours after
960 transfection by filtering through a 0.45 µm filter unit. 50 to 100 µl viral particles were used to
961 transduce target cells grown in 6-well plates in the presence of 8 µg/ml polybrene. 24 hours
962 after transduction, puromycin was added to the medium at a final concentration of 2 µg/ml for
963 HeLa and A549 cells to select for shRNA-expressing cells. Cells were expanded into media
964 containing 1 µg/ml of puromycin for maintenance after two days of selection.

965

siRNA-mediated knockdown

967 All siRNAs were ordered from Sigma-Aldrich, either predesigned or customized. MISSON
968 siRNA Universal Negative Control #1 (SIGMA, SC001) was used as a negative control. The
969 sequences of the used siRNAs are listed in Table S4. siRNAs were transfected with
970 Lipofectamine RNAiMAX (Invitrogen, 13778150) at a final concentration of 15 nM following the
971 manufacturer's instructions. Cells were harvested three days after transfection for Western
972 blotting or live cell imaging.

973

CRISPR-Cas9-mediated knockin of GFP or NG

975 mGFP-FXR1 or mNG-FXR1 knockin cells. Three gRNAs were designed with CRISPOR and
976 ordered from IDT[68]. All three gRNAs worked efficiently and generated mGFP-FXR1 expressing
977 cells with an indistinguishable microscopic distribution of the endogenous fusion protein. All
978 reported knockin cell lines in this work were generated with sgRNA1 (Table S4). The repair
979 donor gBLOCK was designed to include the desired tag (mGFP or mNeonGreen) with a 500 bp
980 overhang on each side for homologous recombination. The donor sequences are listed in Table
981 S4). Silent mutations disrupting the PAM sequences of all three gRNAs were introduced. The
982 gBLOCK was synthesized at Genewiz and cloned into pUC-GW-AMP. The final double-
983 stranded DNA donor was produced using PCR amplification with Q5 HF DNA polymerase
984 (NEB, M0491) and the forward and reverse oligos (KI-donor-F and KI-donor-R) (Table S4).

985 For transfection, cells were seeded in 12-well plates one day ahead. 1.25 µg Cas9 protein (IDT
986 #1078728) and 315 ng sgRNA (IDT synthesized) were mixed with 125 µl Opti-MEM for 10
987 minutes (min). Up to 2.5 µg dsDNA donor and 4 µl TranxIT X2 transfection reagent (Mirus,
988 MIR6003) were added to the mixture, incubated for 15 min at room temperature, and added to
989 HeLa, HEK293T, or A549 cells. Transfected cells were submitted to FACS sorting at least five
990 days after transfection to collect mGFP- or mNeonGreen-positive cells. GFP-positive bulk cells
991 were used. Successful knockin was confirmed with confocal microscopy, western blotting, and
992 genotyping, followed by sequencing. The primers used for genotyping are listed in Table S4.

993

Mutation of endogenous FXR1 using base editing

995 To disrupt the first coiled-coil domain of human FXR1 in A549 cells, base editing was used to
996 change N202 to S202. Adenine Base Editor ABEmax(7.10)-SpG-P2A-EGFP was expressed
997 from the Addgene plasmid #140002[69]. FXR1 exon 7 specific sgRNAs were designed with
998 CRISPOR[68] and expressed from the backbone BPK1520 (Addgene #65777) driven by the U6
999 promoter. DNA oligos used for cloning are listed in Table S4. gRNAs were annealed and
1000 phosphorylated, then ligated into BsmBI-digested and dephosphorylated BPK1520 backbone.

1001 Transfections were performed between 20 and 24 hours after seeding 4 x 10^5 HEK293T or
1002 A549 cells in 6-well plates. 1.4 µg of base-editor and 600 ng of sgRNA expression plasmids
1003 were mixed with 15 µl of TransIT-X2 (Mirus, MIR6003) in a total volume of 300 µl Opti-MEM,
1004 incubated for 15 min at room temperature and added to A549 cells. Transfected cells were
1005 submitted to FACS sorting five days after transfection to collect GFP-positive cells. To perform
1006 FACS sorting, cells in 10 cm dishes were washed with PBS and trypsinized with 2 ml trypsin at
1007 room temperature for 5 min. After carefully removing trypsin, the cells were resuspended in 2 ml
1008 FACS buffer (growth media containing 2.5% FBS) and passed through a cell strainer. GFP-
1009 positive cells were sorted in bulk and 96-well plates with one cell per well on a BD
1010 FACSymphony™ S6 cell sorter.

1011 To assess base editing efficiency, one week after sorting, genomic DNA was extracted using
1012 QuickExtract DNA extraction solution (LGC, SS000035-D2) from the bulk sorted cells.
1013 CRISPRseq DNA was PCR amplified with Q5 (NEB) using oligos listed in Table S4, ran on an
1014 agarose gel, and gel purified using QIAquick Gel Extraction Kit. CRISPRseq results were
1015 processed using the CRISPRESSO2 pipeline[70]. Single cell-derived clones were obtained
1016 through FACS sorting, expanded, and genotyped with Sanger sequencing. For Sanger
1017 sequencing, the forward oligo for amplicon generation was used as the sequencing primer. Two
1018 WT control *FXR1* clonal cell lines, three heterozygous *FXR1-WT/FXR1-N202S*, and one
1019 homozygous *FXR1-N202S/FXR1-N202S* cell line were generated and used in this study.

1020

Mutation of endogenous FXR1 using prime editing

1022 Prime editing was employed to install the mutation FXR1-G266E at the endogenous locus in
1023 A549 cells. Prime editor PEmax with P2A-EGFP was expressed from the addgene plasmid
1024 #180020. The epegRNA was designed with PE-designer[71] and expressed from the backbone
1025 pU6-tevopreq1-GG-acceptor (Addgene # 174038) driven by the U6 promotor. The extra nicking
1026 gRNA was expressed from the backbone LsgRNA (Addgene #47108).

1027 Transfections were performed between 20 and 24 hours after seeding 4×10^5 cells in 6-well
1028 plates. 4 µg of prime editor, 1.3 µg of epegRNA, and 440 ng of nicking gRNA expression
1029 plasmids were mixed with 10 µl of TransIT-X2 (Mirus, MIR6003) in a total volume of 300 µl Opti-
1030 MEM, incubated for 15 min at room temperature and added to A549 cells. Transfected cells
1031 were submitted to FACS sorting five days after transfection to collect GFP-positive cells. GFP-
1032 positive cells were sorted in 96-well plates with one cell per well on a BD FACSymphony™ S6
1033 cell sorter.

1034 To genotype the resulting single cell-derived clones, amplicons were generated with oligos
1035 FXR1-KH1-F and FXR1-KH1-R (listed in Table S4). The PCR products were sequenced using
1036 the oligo FXR1-KH1-F with Sanger sequencing. Three WT control FXR1 clonal cell lines and
1037 two heterozygous *FXR1-WT/FXR1-G266E* cell lines were generated and used in this study.

1038

Immunofluorescence staining

1040 Cells were seeded in 4-well chamber slides (Millipore, PEZGS0416). Specifically, for HEK293T
1041 cells, the chambers were coated with 0.01% Poly-L-lysine (Sigma, P4707) at room temperature
1042 for one hour before seeding. The day after, cells were washed in PBS ($-Ca^{2+}$, $-Mg^{2+}$), fixed in 4%
1043 PFA for 10 min at room temperature, and washed twice with PBS. The cells were then
1044 permeabilized in 0.1% Triton X-100 in PBS for 7 min. After washing three times with PBST (PBS
1045 with 0.1% Tween-20), the cells were incubated in the blocking buffer (3% BSA in PBST) for 1
1046 hour. The cells were then incubated in primary antibody diluted in the blocking buffer for 3 hours
1047 at room temperature or overnight at 4°C. After washing the cells three times in PBST, the cells
1048 were incubated with secondary antibody diluted at 1:1000 in blocking buffer for 1 hour. The cells
1049 were washed three times with PBST and mounted in ProLong Gold Antifade Mountant with
1050 DAPI (Invitrogen, P36941) with precision cover glasses No. 1.5H (Marienfeld, 0107222). All
1051 antibodies are listed in the Key Resource Table.

1052

Confocal microscopy

1054 Two confocal microscopes were used depending on the availability. Most live cell imaging was
1055 conducted on the ZEISS LSM880 confocal laser scanning microscope in Airyscan mode at 37°C
1056 with a Plan-Apochromat 63x/1.4 Oil objective (Zeiss), driven by ZEN black. Exceptions are data

1057   shown in Fig. 3I and Supplemental Videos S1-S6, which were acquired with a SoRa spinning
1058   disk microscope. Most fixed samples were imaged with a SoRa spinning disk microscope. The
1059   SoRa spinning disk was equipped with an ORCA-Fusion BT Digital CMOS camera (C15440-
1060   20UP, Hamamatsu), a motorized piezo stage, and 63x/1.40 CFI Plan Apo oil immersion
1061   objective, driven by the software NIS-ELEMENTS (Nikon).

1062   For live cell imaging with LSM880, including FRAP experiments, cells were seeded in 4-well
1063   Nunc Lab-Tek II chambered coverglasses (Thermo Scientific, 155360) and transfected with
1064   constructs with the above-mentioned amount. Fourteen to 17 hours after transfection, cells were
1065   mounted on the stage housed in a live cell imaging chamber (Zeiss) at 37°C and 5% CO2. Z
1066   stack images were captured with an interval size of 160 nm when applicable. Excitations were
1067   performed sequentially using 405, 488, 594, or 633 nm laser, and imaging conditions were
1068   experimentally optimized to minimize bleed-through. For live cell imaging with SoRa, the cells
1069   were seeded in Ibidi μ-Slide 4-well chambers (Ibidi USA, NC0685967) using FluoroBrite™
1070   DMEM (Gibco, A1896701). The samples were excited with the 488 nm laser and exposed for 80
1071   ms. Raw images are presented unless otherwise stated.

1072   <u>Imaging after RNase A treatment.</u> The cells were seeded in a glass-bottomed 4-well chamber
1073   and transfected with 50 ng mGFP-FXR1-N2 construct. 15 hours after transfection, the cells
1074   were washed twice with PBS, then washed once more with "transport buffer", which contains 20
1075   mM HEPES pH 7.4, 100 mM potassium acetate, 3.5 mM magnesium acetate, 1 mM EGTA, and
1076   250 mM sucrose. The cells were permeabilized with 500 μl of the above-mentioned buffer
1077   containing 50 μg/ml digitonin for 1 min. The cells were washed twice with PBS and incubated in
1078   PBS supplemented with or without 1 mg/ml RNase A (Sigma-Aldrich, Cat# R4642). The signal
1079   obtained from the GFP-FXR1-N2 construct was recorded with the ZEISS LSM880 confocal
1080   laser scanning microscope. At 30 min post RNase A addition, the assembled network was fully
1081   dissociated into spherical granules.

1082   <u>Fluorescence recovery after photobleaching (FRAP).</u> HeLa cells were seeded in 4-well Nunc
1083   Lab-Tek II chambered coverglass (Thermo Scientific, 155360). FRAP experiments were
1084   performed with ZEISS LSM880 in the airyscan mode using the 488 nm laser. A square area of
1085   0.5 x 0.5 μm^2 was bleached with maximal power. For full-length FXR1, the bleaching area was
1086   1.6 x 1.6 μm^2. The fluorescence signal was acquired at the maximum speed possible for 100
1087   seconds at an interval of 2 seconds. The fluorescence intensity of the bleached area was
1088   extracted with ZEN software black edition (ZEISS). The prebleached fluorescence intensity was
1089   normalized to one, and the signal after bleach was normalized to the pre-bleach level. No
1090   photobleaching was observed on non-bleached areas; we therefore took the Plateau values as
1091   mobile fractions.

1092   <u>Three-dimensional colocalization.</u> FMR1 and FXR1 were stained in HeLa cells, and stacks of
1093   images were acquired with a step size of 0.2 μm on a SoRa spinning disk microscope. A
1094   63x/1.40 CFI Plan Apo oil immersion objective and a 4x magnification changer for SoRa were
1095   used. Images were deconvolved with default settings using NIS-elements software. These
1096   images were then imported into Imaris software and automatically thresholded. The '3D coloc'
1097   function was applied to all volumes and generated related parameters, including the percentage
1098   of volume colocalized for FMR1 and FXR1, as well as the Person's correlation coefficient in the
1099   thresholded volume.

1100   <u>Connected component analysis</u>. Confocal images of GFP-FXR1-N1 or -N2 were acquired with
1101   either LSM880 or SoRa. The images were then analyzed in Python with scikit-image[72]. Briefly,
1102   the images were automatically thresholded and the connected components, which are called
1103   objects in this paper, were identified using the 'skimage.measure' function with the connectivity

1104 specified as 2. These objects were then assigned random colors. Each object's size (area) and
1105 the total number of objects per cell were extracted.

1106

RhoA pathway stimulation and stress fiber staining

1108 A549 cells were seeded in 4-well chamber slides (Millipore, PEZGS0416) at a density of 0.03
1109 x10^6 cells per well. The evening after, the cells were washed twice with starvation media
1110 (DMEM-HG without FBS) and incubated in 500 µl starvation media for 17 hours. The cells were
1111 stimulated with 3 µM LPA (Avanti, 857130P) or 60 nM thrombin (Novagen, 69671). 30 min after
1112 stimulation, the cells were washed with PBS and fixed in 4% PFA for 10 min at room
1113 temperature. Filamentous actin was stained with Phalloidin-iFluor 555 Reagent (Abcam,
1114 ab176756) per the manufacturer's instructions. The presence of stress fibers for each cell was
1115 scored either positive or negative. A fraction of the dataset was blindly scored by two authors,
1116 and a similar fraction of stress fiber-positive cells was found. Most of the images were scored by
1117 the first author.

1118 For western blot analysis, cells were seeded in 6-well plates lysed in 1x reducing Laemmli SDS
1119 sample buffer 15 min after stimulation unless otherwise stated.

1120

Active RhoA pulldown

1122 Active RhoA pulldown was performed with the RhoA Pull-Down Activation Assay Kit
1123 (Cytoskeleton, Inc, BK036-S), following the manufacturer's instructions. Briefly, A549 cells were
1124 seeded in 6 cm dishes and serum-starved for 17 hours. The cells were then stimulated with or
1125 without 3 µM LPA for 5 min before washing and lysing. Active RhoA was enriched by GST-
1126 tagged Rhotekin-RBD protein coupled to agarose beads. The beads were thoroughly washed,
1127 and the resulting products were separated on SDS-PAGE and analyzed using Western blotting.

1128

Proximity ligation assay

1130 A549 cells were seeded onto glass coverslips (Fisherbrand, 12541001, No 1.5) with a 12 mm
1131 diameter placed in 24-well plates. The cells were serum-starved for 17 hours before stimulation.
1132 10 min after 60 nM thrombin stimulation, cells were fixed with 4% PFA in PBS for 10 min,
1133 permeabilized with 0.1% Triton in PBS for 7 min, washed with PBST three times, blocked in 3%
1134 BSA in PBS for 30 min, and incubated with primary antibody diluted in blocking buffer overnight
1135 at 4°C. The next day, cells were washed with PBST three times and incubated with secondary
1136 antibody with PLUS and MINUS DNA probes (Sigma-Aldrich, DUO92102) for 1 hour at 37°C.
1137 Washed with Wash Buffer A two times, incubated in ligation mix for 30 min at 37°C. Washed
1138 with Wash Buffer A two times, incubated in signal amplification mix for 100 min at 37°C. Finally,
1139 washed with Wash Buffer B two times, and with 0.01 x Wash Buffer B once. Cells were then
1140 mounted in Prolong Gold Antifade Mountant with DAPI for imaging on a confocal microscope. Z-
1141 section images (N = 21) separated by 0.4 µm increments were captured. Images were analyzed
1142 in ImageJ with a custom script. Briefly, images were max-z projected and auto-thresholded. The
1143 dots were then selected with the 'find maxima' function and counted for individual cells with
1144 manually drawn regions of interest (ROIs) using the ROI manager.

1145

Migration assay

1147 6,000 serum-starved A549 cells in 100 µl serum-free DMEM were dispensed into the transwell
1148 insert in a 24-well plate (Costar 3422, 8 µm pore size) with 500 µl complete DMEM. When used,

1149 ROCK inhibitor Y-27632 (Catalog # 72307, STEMCELL technologies) was added at a final
1150 concentration of 10 µM for two hours prior to dispensing into transwell inserts. And fresh ROCK
1151 inhibitor was added to the transwells for the whole duration of the experiment. The wells, and
1152 the inserts were washed with PBS 20 hours after seeding. 500 µl accutase (Innovative Cell
1153 Technologies, AT-104) was added to the wells and incubated at room temperature for 8
1154 minutes. Cells in the accutase solution were collected by centrifugation and subjected to
1155 Cyquant (Invitrogen, C7026) based DNA quantity measurement using a plate reader
1156 SpectraMax iD5 and clear bottom black assay plates (Costar, 3603).

1157

Size exclusion chromatography

1159 8×10^6 HeLa cells or A549 cells were lysed in 550 µl mild lysis buffer containing 50 mM HEPES,
1160 pH 7.4, 150 mM NaCl, 0.5% NP40, 1 mM PMSF, and 1 x EDTA-free Protease Inhibitor Cocktail
1161 (Roche). The cells were further broken down with six passes through a 27-gauge needle. The
1162 lysate was cleared at top speed for 10 min with a tabletop centrifuge at 4°C. 500 µl crude lysate
1163 was loaded into the Superose® 6 Increase 10/300 GL column (Cytiva, 29091596) driven by an
1164 AKTA FPLC system (GE Healthcare). 1 ml fractions were collected over the entire run. 200 µl
1165 100% (w/v) TCA (SIGMA, T9159) was added to each fraction and kept at -80°C overnight. The
1166 precipitated protein was collected and washed twice with 1 ml of ice-cold acetone. Finally,
1167 protein was airdried and resuspended in 120 µl 2x reducing Laemmli SDS sample buffer. These
1168 samples were further analyzed using western blotting.

1169 When fractionating GFP-FXR1 WT and CC mutant fusion proteins, instead of TCA precipitation,
1170 150 µl of each collected fraction was loaded into a 96-well solid black microplate (Corning,
1171 3915) and analyzed with an Infinite M1000 plate reader (Tecan). Fluorescence was collected
1172 with top reading mode, excited at 488 nm, and collected at 510 ± 5 nm with optimal gain. A GFP
1173 negative lysate sample from the same cell type was fractionated and served as background
1174 control for the autofluorescence.

1175

Co-immunoprecipitation

1177 GFP trap (Chromotek, Gta-100) co-IP was performed as follows. HeLa cells were transfected
1178 with constructs expressing GFP or GFP-fusion proteins, as described above. About 17 hours
1179 after transfection, the cells were washed with PBS twice and drained of the remaining liquid.
1180 The cells were scrapped into 700 µl lysis buffer containing 50 mM HEPES, pH 7.4, 150 mM
1181 NaCl, 1% NP40, 0.5% sodium deoxycholate, 0.05% SDS, 1 mM EDTA, 1 x EDTA-free protease
1182 inhibitor cocktail (Roche). The cells were lysed on ice for 30 min. After centrifugation at 21,130 g
1183 for 10 min, GFP-trap co-IP was performed following the manufacturer's instructions with 15 µl
1184 slurry per reaction. GFP-trap beads were added, incubated with cell lysate for 1 to 2 hours at
1185 4°C on a rotator, and washed four times with ice-cold wash buffer containing 50 mM HEPES,
1186 pH 7.4, 150 mM NaCl, and 1 mM EDTA.

1187 When RNase A treatment was required, the beads were split into two samples after the third
1188 wash and resuspended in 200 µl of wash buffer. A final concentration of 30 mg/ml of RNase A
1189 (Sigma-Aldrich, Cat# R4642) was added and treated at room temperature for 30 min. After a
1190 final wash, the GFP-trap beads were mixed with 2x Laemmli sample buffer, boiled at 95°C for 5
1191 min, and subjected to Western blotting.

1192

Western blotting

1194 Cells were washed with PBS and lysed with 1x reducing Laemmli SDS sample buffer (Thermo
1195 Scientific Chemicals, J60015-AC) to generate whole cell lysate. The viscous products were
1196 transferred to Eppendorf tubes and boiled at 95°C for 15 min.

1197 For co-immunoprecipitation experiments, proteins were eluted from beads by boiling in 2x
1198 reducing Laemmli SDS sample buffer at 95°C for 5 min.

1199 Denatured protein samples were separated in 4%-12% NuPAGE Bis-Tris gels (Invitrogen) and
1200 wet-transferred to nitrocellulose membranes with X cell II blot module (Invitrogen). For analyzing
1201 high molecular weight proteins such as Myosin (MYH9), samples were separated in 3% - 8%
1202 Tris-Acetate gels (Invitrogen) with NuPAGE Tris-Acetate SDS Running buffer. Membranes were
1203 blocked with Odyssey blocking buffer (LI-COR) or 5% non-fat milk in TBST (exclusively when
1204 blotting RLC and pRLC) and then incubated with primary antibody at 4°C overnight. Membranes
1205 were washed three times with PBST (0.1% Tween) and incubated with dye-labeled secondary
1206 antibody. Membranes were scanned with the Odyssey DLx system (LI-COR). All antibodies are
1207 listed in the Key Resource Table.

1208

1209 **Oligo(dT) pulldown of mRNA-associated proteins without cross-linking**

1210 Plasmids expressing GFP-fusion proteins were transfected into U2OS *FXR1/FXR2/FMR1* triple
1211 knockout cells one day ahead. About 6 x 10^6 U2OS were harvested for each reaction. For A549
1212 cells with endogenous FXR1-N202S or FXR1-G266E mutation, the cells were seeded one day
1213 ahead to reach 70% confluency the next day for harvesting. Cells were washed with ice-cold
1214 PBS and lysed in 0.7 ml ice-cold lysis buffer containing 50 mM HEPES, pH 7.4, 150 mM NaCl,
1215 1% NP40, 0.5% sodium deoxycholate, 0.05% SDS, 1 mM EDTA, and 1 x protease inhibitor
1216 cocktail (Roche). Samples were further lysed with forty strokes of a chilled dounce
1217 homogenizer. Lysates were cleared at 21,000 x g for 10 min at 4°C. 30 µl oligo(dT)25 magnetic
1218 beads (NEB, S1419S) were equilibrated in wash buffer containing 50 mM HEPES, pH 7.4, 150
1219 mM NaCl, and 1 mM EDTA. The cleared lysate was mixed with the beads and was rotated for
1220 60 min at 4°C. Samples were washed four times with 0.7 ml wash buffer and eluted from the
1221 beads with 2x reducing Laemmili sample buffer at 95°C for 5 min. The samples were analyzed
1222 using western blotting.

1223

1224 **RNA immunoprecipitation without cross-linking**

1225 RNA immunoprecipitation assays were used to validate iCLIP results. 8 x 10^6 HeLa cells per
1226 condition were homogenized in lysis buffer containing 50 mM HEPES, pH 7.4, 150 mM NaCl,
1227 1% NP40, 0.5% sodium deoxycholate, 0.05% SDS, 1 mM EDTA, 1 x EDTA-free protease
1228 inhibitor cocktail (Roche), and 2 U/ml SUPERase•In™ RNase Inhibitor (Invitrogen). Cleared
1229 lysates were incubated with 10 µg anti-FXR1 antibody (Novus #NBP2-22246) or Rabbit IgG
1230 (Cell Signaling Technologies #2729)-coupled protein A beads for four hours at 4°C. After
1231 washing the beads three times with wash buffer containing 50 mM HEPES pH 7.4, 150 mM
1232 NaCl, and 0.05% NP40, RNA was eluted from the beads with 1 mg/ml proteinase K (AM2546)
1233 at 50°C for 40 min. RNA was then isolated with TRI reagent (Invitrogen) with standard
1234 procedure and reverse transcribed using qScript cDNA SuperMix (Quantabio). The primer
1235 sequences for RT-qPCR analysis are listed in Table S4. Enrichment relative to input RNA was
1236 calculated using cycle threshold values for each mRNA. The final fold change of FXR1/IgG was
1237 obtained by dividing the enrichment over input of FXR1-IP by IgG-IP.

1238

1239 **SILAC mass spectrometry**

1240   HeLa cells stably expressing shRNAs against FXR1 were cultivated in DMEM medium (Thermo
1241   Scientific, A33822) supplemented with 10% dialyzed FBS (Gibco, 26400044) and 1% penicillin
1242   and containing either "light" (L-Arginine-HCL (Thermo Scientific, 89989), L-Lysine-2HCL
1243   (Thermo Scientific, 89987)) or "heavy" (L-Arginine-HCL (13C6, 99%; 15N4, 99%; Cambridge
1244   Isotope Laboratories, CNLM-539-H-0.05, L-Lysine-2HCL (13C6, 99%; Thermo Scientific,
1245   1860969)) stable isotope labeled amino acids. Cells were cultivated for at least six passages
1246   before the incorporation efficiency was verified by mass spectrometry analysis to be above
1247   99%.

1248   The 'light' HeLa cells were transfected with GFP-FXR1a (containing a silent mutation that
1249   makes it shRNA-resistant), and the 'heavy' cells were transfected with shRNA-resistant GFP-
1250   FXR1a-CC2 mutant (V361P) using Lipofectamine 2000. After 18 hours, transfected cells were
1251   collected and lysed in buffer containing 50 mM Tris–HCl pH 7.5, 150 mM NaCl, 1% Triton X-
1252   100, 1 mM EDTA, 0.25% sodium deoxycholate, and 1x protease inhibitor cocktail (Roche,
1253   11836153001). GFP-trap (Chromotek, Gta-100) co-IP was performed separately using light and
1254   heavy lysates. 30 µl slurry per sample was used. The resulting beads were pooled and mixed
1255   with 2x Laemmli sample buffer followed by SDS-gel electrophoresis in MES running buffer using
1256   4-12% Bis-Tris NuPAGE gels at 120 V for 10 min. Following the manufacturer's instructions, the
1257   protein gels were stained with SimplyBlue (Life Technologies) and submitted to the MSKCC
1258   Proteomics Core facility for SILAC mass spectrometry analysis.

1259   The samples were divided into three gel slices (Fig. S7A), and all three gel slices were
1260   processed for MS analysis. They were washed with 1:1 (Acetonitrile:100 mM ammonium
1261   bicarbonate) for 30 min, dehydrated with 100% acetonitrile for 10 min, excess acetonitrile was
1262   removed, and slices were dried in speed-vac for 10 min without heat. Gel slices were reduced
1263   with 5 mM DTT for 30 min at 56°C in a thermomixer (Eppendorf), chilled to room temperature,
1264   and alkylated with 11 mM IAA for 30 min in the dark. Gel slices were washed with 100 mM
1265   ammonium bicarbonate and 100% acetonitrile for 10 min each. Excess acetonitrile was
1266   removed and dried in speed-vac for 10 min without heat, and gel slices were rehydrated in a
1267   solution of 25 ng/µl trypsin in 50 mM ammonium bicarbonate on ice for 30 min. Digestions were
1268   performed overnight at 37°C in a thermomixer. Digested peptides were collected and further
1269   extracted from gel slices in an extraction buffer (1:2 (v/v) 5% formic acid/acetonitrile) at high-
1270   speed shaking in a thermomixer. Supernatant from both extractions was combined and dried in
1271   a vacuum centrifuge. Peptides were desalted with C18 resin-packed stage tips, lyophilized, and
1272   stored at -80°C until further use.

1273   <u>LC-MS/MS analysis:</u> Desalted peptides were dissolved in 3% acetonitrile/0.1% formic acid and
1274   were injected onto a C18 capillary column on a nano ACQUITY UPLC system (Water), which
1275   was coupled to the Q Exactive plus mass spectrometer (Thermo Scientific). Peptides were
1276   eluted with a non-linear 200 min gradient of 2-35% buffer B (0.1% (v/v) formic acid, 100%
1277   acetonitrile) at a 300 nl/min flow rate. After each gradient, the column was washed with 90%
1278   buffer B for 5 min and re-equilibrated with 98% buffer A (0.1% formic acid, 100% HPLC-grade
1279   water). MS data were acquired with an automatic switch between a full scan and 10 data-
1280   dependent MS/MS scans (TopN method). The target value for the full scan MS spectra was 3 x
1281 10^6 ions in the 380-1800 m/z range with a maximum injection time of 30 ms and resolution of
1282   70,000 at 200 m/z with data collected in profile mode. Precursors were selected using a
1283   1.5 m/z isolation width. Precursors were fragmented by higher-energy C-trap dissociation (HCD)
1284   with a normalized collision energy of 27 eV. MS/MS scans were acquired at a resolution of
1285   17,500 at 200 m/z with an ion target value of 5 x 10^4, maximum injection time of 60 ms, dynamic
1286   exclusion for 15 s and data collected in centroid mode.

1287

Tandem Mass Tag (TMT) Multiplexed Quantitative Mass Spectrometry

The TMT analysis was performed with four replicates per sample. 4×10^6 HeLa cells expressing control shRNA or an shRNA against FXR1 were used as samples. Cells were trypsinized and washed three times with ice-cold PBS. Pelleted cells were snap-frozen in liquid nitrogen after the final wash. Cell pellets were lysed with 200 µl buffer containing 8 M urea and 200 mM EPPS pH = 8.5, with protease inhibitor (Roche) and phosphatase inhibitor cocktails 2 and 3 (Sigma). Benzonase (Millipore) was added to a concentration of 50 µg/ml and incubated at room temperature for 15 min followed by water bath sonication. Samples were centrifuged at 4°C, 14,000 g for 10 min, and the supernatant was extracted. BCA assay (Pierce) was used to determine the protein concentration. Protein disulfide bonds were reduced with 5 mM tris (2-carboxyethyl) phosphine at room temperature for 15 min, then alkylated with 10 mM iodoacetamide at room temperature for 30 min in the dark. The reaction was quenched with 10 mM dithiothreitol, incubated at room temperature for 15 min. Aliquots of 100 µg were taken for each sample and diluted to approximately 100 µl with lysis buffer. Samples were subjected to chloroform/methanol precipitation as previously described[73]. Pellets were reconstituted in 200 mM EPPS buffer and digested with Lys-C (1:50 enzyme-to-protein ratio) and trypsin (1:50 enzyme-to-protein ratio) at 37°C overnight.

Peptides were TMT-labeled as described[73]. Briefly, peptides were TMT-tagged by adding anhydrous ACN and TMTPro reagents (16plex) for each respective sample and incubated for one hour at room temperature. A ratio check was performed by taking a 1 µl aliquot from each sample and desalted by StageTip method[74]. TMT tags were then quenched with hydroxylamine to a final concentration of 0.3% for 15 min at room temperature. Samples were pooled 1:1 based on the ratio check and vacuum-centrifuged to dryness. Dried peptides were reconstituted in 1 ml of 3% ACN/1% TFA, desalted using a 100 mg tC18 SepPak (Waters), and vacuum-centrifuged overnight.

Peptides were centrifuged to dryness and reconstituted in 1 ml of 1% ACN/25mM ABC. Peptides were fractionated into 48 fractions. An Ultimate 3000 HPLC (Dionex) coupled to an Ultimate 3000 Fraction Collector using a Waters XBridge BEH130 C18 column (3.5 µm 4.6 x 250 mm) was operated at 1 ml/min. Buffer A, B, and C consisted of 100% water, 100% ACN, and 25 mM ABC, respectively. The fractionation gradient operated as follows: 1% B to 5% B in 1 min, 5% B to 35% B in 61 min, 35% B to 60% B in 5 min, 60% B to 70% B in 3 min, 70% B to 1% B in 10min, with 10% C the entire gradient to maintain pH. The 48 fractions were then concatenated to 12 fractions, (i.e. fractions 1, 13, 25, 37 were pooled, followed by fractions 2, 14, 26, 38, etc.) so that every 12th fraction was used to pool. Pooled fractions were vacuum-centrifuged and then reconstituted in 1% ACN/0.1% FA for LC-MS/MS.

Fractions were analyzed by LC-MS/MS using a NanoAcquity (Waters) with a 50 cm long (inner diameter 75 µm) EASY-Spray Column (PepMap RSLC, C18, 2 µm, 100 Å) heated to 60°C coupled to an Orbitrap Eclipse Tribrid Mass Spectrometer (Thermo Fisher Scientific). Peptides were separated by direct injection at a flow rate of 300 nl/min using a gradient of 5 to 30% acetonitrile (0.1% FA) in water (0.1% FA) over three hours and then to 50% ACN in 30 min and analyzed by SPS-MS3. MS1 scans were acquired over a m/z 375-1500 range, 120K resolution, AGC target (standard), and maximum IT of 50 ms. MS2 scans were acquired on MS1 scans of charge 2-7 using isolation of 0.5 m/z, collision-induced dissociation with activation of 32%, turbo scan, and max IT of 120 ms. MS3 scans were acquired using specific precursor selection (SPS) of 10 isolation notches, m/z range 110-1000, 50K resolution, AGC target (custom, 200%), HCD activation of 65%, max IT of 150 ms, and dynamic exclusion of 60 s.

FXR1 iCLIP

1336 HeLa cells were seeded in 10 cm dishes to reach 70% confluency the next day. After 24 hours,
1337 cells were transfected with either mGFP-FXR1-WT or mGFP-FXR1-CC2mut, as described in
1338 the transfections section.

1339 20 hours after transfection, cells were rinsed once with ice-cold PBS and 6 ml of fresh PBS was
1340 added to each plate before proceeding to the improved iCLIP protocol[75], with the following
1341 details. Cells were irradiated once with 150 mJ/cm^2 in a Spectroline UV Crosslinker at 254 nm.
1342 Irradiated cells were scraped into Eppendorf tubes, spun at 500 x g for one minute, and snap-
1343 frozen in liquid nitrogen. Crosslinked cell pellets were lysed in iCLIP lysis buffer (50 mM Tris-
1344 HCl pH 7.4, 100 mM NaCl, 1% Igepal CA-630 (Sigma I8896), 0.1% SDS, 0.5% sodium
1345 deoxycholate, Complete protease inhibitor cocktail (Roche, 5056489001) and sonicated with the
1346 Bioruptor Pico for 10 cycles 30 seconds ON/30 seconds OFF. For RNA fragmentation, 4 U of
1347 Turbo DNase (Ambion, AM2238) and 0.1 U of RNase I (Thermo Scientific, EN0601) were added
1348 per 1 mg/ml lysate. Lysates were pre-cleared by centrifugation at 20,000 x g at 4°C. A mix of
1349 Protein G Dynabeads (100 µl per sample, Life Technologies) was coupled to 4 µg of rabbit anti-
1350 GFP antibody (Abcam ab290) and used for FXR1 protein-RNA complexes immunoprecipitation.
1351 Bead bound complexes were washed with high salt (50 mM Tris-HCl, pH 7.4, 1 M NaCl, 1 mM
1352 EDTA, 1% Igepal CA-630 (Sigma I8896), 0.1% SDS, 0.5% sodium deoxycholate) and PNK
1353 wash buffer (20 mM Tris-HCl, pH 7.4, 10 mM MgCl2, 0.2% Tween-20). RNA was first
1354 dephosphorylated and then ligated to a pre-adenylated infra-red labeled L3-IR adaptor on
1355 beads[76]. Excess adaptor was removed by incubation with 5′ deadenylase (NEB M0331S) and
1356 the exonuclease RecJf (NEB M0264S). GFP-FXR1 protein-RNA complexes were eluted from
1357 the beads by heating at 70°C for one minute, size-separated with SDS-PAGE, transferred to a
1358 nitrocellulose membrane, and visualized by iBright Imaging Systems via the infrared-labeled
1359 adaptor. RNA was released from the membrane by proteinase K digestion and recovered by
1360 precipitation. cDNA was synthesized with Superscript IV Reverse Transcriptase (Life
1361 Technologies) and circularized by CircLigase II. Circularized cDNA was purified with AMPure
1362 XP beads (A63880, Beckman Coulter), amplified by PCR, size-selected with AMPure beads,
1363 and quality-controlled for sequencing. Libraries were sequenced as single-end 100 bp reads on
1364 Illumina HiSeq 4000.

1365

1366

1367 **Data analysis**

1368 **Protein domains**

1369 Protein disorder prediction. Regions containing IDRs were determined using IUPred2A
1370 prediction program using 'long disorder'[77]. Regions with scores higher than 0.5 are considered
1371 disordered.

1372 Coiled-coil domain prediction. CC domains were predicted using the 'coils' program. A CC
1373 domain was predicted when the coils score was greater than 0.2. Proteins with predicted CC
1374 domains are listed in Table S1. Based on these criteria, 4168 (out of 8901 expressed genes) in
1375 HeLa cells encode proteins with at least one predicted CC domain. The resulting expected
1376 frequency of CC domains is 0.468. As this prediction program is no longer available, CC
1377 domains were also determined using the Ncoils tool implemented at the waggawagga server[35].
1378 Several other tools were employed by the server simultaneously for high-confidence prediction.
1379 The CC domains shown in Figures 2A, 3A, 7A, and 7B were based on predictions from the
1380 Ncoils tool with a minimum window length of 21 aa.

1381 <u>Tudor domains.</u> Tudor domains were obtained from UniProt and are listed in Table S1. In HeLa
1382 cells, 79 genes encode proteins with at least one Tudor domain, resulting in an expected
1383 frequency of Tudor domains of 0.0088.

1384 <u>RG/RGG domains.</u> These domains were obtained from Thandapani et al., (2013)[29] and contain
1385 at least two neighboring RG repeats or two neighboring RGG repeats. They are listed in Table
1386 S1. Among the proteins expressed in HeLa cells, 600 contain RG/RGG domains, resulting in an
1387 expected frequency of RG/RGG domains of 0.067.

1388 <u>Protein domain enrichment.</u> To determine whether a protein domain is considered enriched
1389 among the FXR1 network-dependent interactors, we calculated the observed over expected
1390 frequency of CC, Tudor, or RG/RGG domains. The expected frequency is the frequency of
1391 domains observed in HeLa cells. The observed frequency of protein domains was obtained from
1392 the top 20% of most FXR1 network-dependent protein interactors. These proteins have the
1393 lowest log2 FC of FXR1-CC2mut/FXR1-WT. A Chi-square test was performed to test if the
1394 enrichment is statistically significant (Table S3).

1395

1396 **Protein sequence conservation analysis**

1397 Sequence conservation was calculated by computing the global alignment across 375
1398 (metazoa) orthologous FXR1 sequences identified using the EggNog server[78]. Alignment was
1399 performed using Clustal Omega, and conservation was determined using the default analysis
1400 for conservation in JalView[79].

1401

1402 **Gene ontology analysis**

1403 Gene ontology analysis was performed with FXR1 network dependent mRNA targets using
1404 DAVID[46].

1405

1406 **mRNA abundance of FXR family proteins across cell types**

1407 The values were obtained from the Human Cell Landscape
1408 (https://db.cngb.org/HCL/data/HCL_102_average_expression.xlsx)[23].

1409

1410 **TMT proteomics data analysis**

1411 For quantitative analysis, raw data files were processed using Proteome Discoverer (PD)
1412 version 2.4.1.15 (Thermo Scientific). For each of the TMT experiments, raw files from all
1413 fractions were merged and searched with the SEQUEST HT search engine with a Homo
1414 sapiens UniProt protein database downloaded on 2019/01/09 (176,945 entries). Cysteine
1415 carbamidomethylation was specified as fixed modifications, while oxidation (M), acetylation of
1416 the protein N-terminus, TMTpro (K) and TMTpro (N-term), deamidation (NQ), and
1417 phosphorylation (S, T, Y) were set as variable modifications. The precursor and fragment mass
1418 tolerances were 10 ppm and 0.6 Da, respectively. A maximum of two trypsin missed cleavages
1419 was permitted. Searches used a reversed sequence decoy strategy to control peptide false
1420 discovery rate (FDR) and 1% FDR was set as the threshold for identification.

1421 The TMT experiment result was plotted as a volcano plot with biological significance defined as
1422 log2 fold change below -1.5 or over 1.5 and -log10 (*P* value) > 3.

1423

1424 **SILAC mass spectrometry data analysis**

1425 SILAC mass spectrometry data were processed using the MaxQuant software (Max Planck
1426 Institute of Biochemistry; v.1.5.3.30). The default values were used for the first search tolerance
1427 and main search tolerance—20 ppm and 6 ppm, respectively. Labels were set to Arg10 and
1428 Lys6. MaxQuant was set up to search the reference human proteome database downloaded
1429 from UniProt on January 9th, 2020. MaxQuant performed the search assuming trypsin digestion
1430 with up to two missed cleavages. Peptide, site and protein FDR were all set to 1% with a
1431 minimum of one peptide needed for identification but two peptides needed to calculate a protein
1432 level ratio. Ratio values of FXR1-CC2mut (H)/FXR1-WT (L) were log2-transformed (Table S3).

1433

1434 **iCLIP data analysis**

1435 The sequencing reads were mapped to hg38, and the number of unique CLIP reads that aligned
1436 to 5′UTRs, coding sequences (CDS), or 3′UTRs were counted. The sum of unique CLIP reads
1437 that were assigned to each specific mRNA correspond to the number of FXR1 binding sites in
1438 said mRNA. According to RNA-seq, in HeLa cells, 8901 genes are expressed with TPM values
1439 greater than 3. Their TPM values are listed in Table S1. Out of 8901 expressed mRNAs, in the
1440 iCLIP sample obtained using WT FXR1, we detected 6697 mRNAs with at least one FXR1
1441 binding site. Among those, the top third of genes had seven or more FXR1 binding sites per
1442 mRNA and these mRNAs were considered FXR1 targets ($N = 2327$, Table S1). The total
1443 number of FXR1 binding sites in the WT sample was 66567, whereas it was 48417 in the
1444 CCmut2 sample. This supports our observation obtained from the oligo(dT) pulldown
1445 experiment that FXR1 dimerization promotes RNA binding. Among the FXR1 targets, we
1446 considered an mRNA to be network-dependent ($N = 1223$), if the number of FXR1 binding sites
1447 per mRNA decreased by at least two-fold, when comparing the WT and CC2mut samples (Fig.
1448 S5F). The remaining FXR1 targets ($N = 1104$) are considered network-independent (Table S1).

1449 Correlation of mRNA features with FXR1 mRNA targets. mRNA length, CDS length and the
1450 percentage of AU (AU-content) were determined using transcripts from the Matched Annotation
1451 from the NCBI and EMBL-EBI (MANE)[80] human version 1.2. For each gene, the transcript with
1452 the longest mRNA length was selected. Protein length was calculated by dividing CDS length by
1453 three. 3′UTR length was obtained from Ref-seq and the longest 3′UTR isoform of each gene
1454 was used (Table S1).

1455

1456 **Statistics**

1457 Statistical parameters are reported in the figures and figure legends, including the definitions
1458 and exact values of N and experimental measures (mean ± std or boxplots depicting median,
1459 25th and 75th percentile (boxes) and 5% and 95% confidence intervals (error bars). Pair-wise
1460 transcriptomic feature comparisons and FRAP sample comparisons were performed using a
1461 two-sided Mann-Whitney test. Enrichment of protein domains was performed using a Chi-
1462 square test. The Pearson P value is reported. When showing bar plots, one-way ANOVA was
1463 performed. Statistical tests were performed on the means of the replicates.

1464
1465

1466 **Supplementary Table and Video Legends**

1467 **Table S1**. FXR1 mRNA targets identified by iCLIP in HeLa cells, related to Figure 4.

1468 **Table S2**. Protein abundance fold changes upon FXR1 knockdown in HeLa cells determined by
1469 TMT mass spectrometry in HeLa cells, related to Figure 5.

1470 **Table S3**. FXR1 network-dependent protein interactors determined by SILAC mass
1471 spectrometry and protein domains enriched among FXR1 interacting proteins, related to Figure
1472 6.

1473 **Table S4**. List of oligos and nucleic acid sequences used in this study, related to STAR
1474 Methods.

1475 **Video S1.** A time-lapse of mGFP-FXR1 full-length protein recorded at an interval of 10 seconds,
1476 related to Figures 1 and 3. Scale bar, 1 μm.

1477 **Video S2.** A time-lapse of mGFP-FXR1 full-length protein recorded at an interval of 2 seconds,
1478 related to Figure 1. Scale bar, 1 μm.

1479 **Video S3.** A time-lapse of mGFP-FXR1-N2 protein recorded at an interval of 10 seconds,
1480 related to Figure 1. Scale bar, 1 μm.

1481 **Video S4.** A time-lapse of mGFP-FXR1-N1 protein recorded at an interval of 10 seconds,
1482 related to Figures 1 and 3. Scale bar, 1 μm.

1483 **Video S5.** A time-lapse of mGFP-FXR1-N1 protein recorded at an interval of 2 seconds, related
1484 to Figure 1. Scale bar, 1 μm.

1485 **Video S6.** A time-lapse of mGFP-FXR1-I304N protein recorded at an interval of 2 seconds,
1486 related to Figure 1. Scale bar, 1 μm.

1487 **Video S7.** A time-lapse of mGFP-FXR1 full-length protein distribution during FRAP, related to
1488 Figure 1. Scale bar, 1 μm.

1489 **Video S8.** A time-lapse of mGFP-FXR1-N1 protein distribution during FRAP, related to Figure 1.
1490 Scale bar, 1 μm.

1491 **Video S9.** A time-lapse of mGFP-FXR1-N2 protein distribution during FRAP, related to Figure 1.
1492 Scale bar, 1 μm.

1493 **Video S10.** A time-lapse of mGFP-FXR1-I304N protein distribution during FRAP, related to
1494 Figure 3. Scale bar, 1 μm.

1495

1496
1497

References

1. Banani, S.F., Lee, H.O., Hyman, A.A., and Rosen, M.K. (2017). Biomolecular condensates: organizers of cellular biochemistry. Nature reviews. Molecular cell biology *18*, 285-298.

2. Peeples, W., and Rosen, M.K. (2021). Mechanistic dissection of increased enzymatic rate in a phase-separated compartment. Nature chemical biology *17*, 693-702.

3. Li, P., Banjade, S., Cheng, H.C., Kim, S., Chen, B., Guo, L., Llaguno, M., Hollingsworth, J.V., King, D.S., Banani, S.F., et al. (2012). Phase transitions in the assembly of multivalent signalling proteins. Nature *483*, 336-340.

4. Su, X., Ditlev, J.A., Hui, E., Xing, W., Banjade, S., Okrut, J., King, D.S., Taunton, J., Rosen, M.K., and Vale, R.D. (2016). Phase separation of signaling molecules promotes T cell receptor signal transduction. Science *352*, 595-599.

5. Kedersha, N.L., Gupta, M., Li, W., Miller, I., and Anderson, P. (1999). RNA-binding proteins TIA-1 and TIAR link the phosphorylation of eIF-2 alpha to the assembly of mammalian stress granules. The Journal of cell biology *147*, 1431-1442.

6. Sheth, U., and Parker, R. (2003). Decapping and decay of messenger RNA occur in cytoplasmic processing bodies. Science *300*, 805-808.

7. Ma, W., and Mayr, C. (2018). A Membraneless Organelle Associated with the Endoplasmic Reticulum Enables 3'UTR-Mediated Protein-Protein Interactions. Cell *175*, 1492-1506 e1419.

8. Luo, Y., Pratihar, S., Horste, E.H., Mitschka, S., Mey, A.S.J.S., Al-Hashimi, H.M., and Mayr, C. (2023). mRNA interactions with disordered regions control protein activity. bioRxiv, 2023.2002.2018.529068.

9. Horste, E.L., Fansler, M.M., Cai, T., Chen, X., Mitschka, S., Zhen, G., Lee, F.C.Y., Ule, J., and Mayr, C. (2023). Subcytoplasmic location of translation controls protein output. Mol Cell *83*, 4509-4523.e4511.

10. Ma, W., Zhen, G., Xie, W., and Mayr, C. (2021). In vivo reconstitution finds multivalent RNA-RNA interactions as drivers of mesh-like condensates. eLife *10*.

11. Siomi, M.C., Siomi, H., Sauer, W.H., Srinivasan, S., Nussbaum, R.L., and Dreyfuss, G. (1995). FXR1, an autosomal homolog of the fragile X mental retardation gene. Embo j *14*, 2401-2408.

12. Guduric-Fuchs, J., Möhrlen, F., Frohme, M., and Frank, U. (2004). A fragile X mental retardation-like gene in a cnidarian. Gene *343*, 231-238.

13. Richter, J.D., and Zhao, X. (2021). The molecular biology of FMRP: new insights into fragile X syndrome. Nat Rev Neurosci *22*, 209-222.

14. Biological insights from 108 schizophrenia-associated genetic loci. (2014). Nature *511*, 421-427.

15. Stepniak, B., Kästner, A., Poggi, G., Mitjans, M., Begemann, M., Hartmann, A., Van der Auwera, S., Sananbenesi, F., Krueger-Burg, D., Matuszko, G., et al. (2015). Accumulated common variants in the broader fragile X gene family modulate autistic phenotypes. EMBO Mol Med *7*, 1565-1579.

16. Pardiñas, A.F., Holmans, P., Pocklington, A.J., Escott-Price, V., Ripke, S., Carrera, N., Legge, S.E., Bishop, S., Cameron, D., Hamshere, M.L., et al. (2018). Common schizophrenia alleles are enriched in mutation-intolerant genes and in regions under strong background selection. Nat Genet *50*, 381-389.

17. Santos-Cortez, R.L.P., Khan, V., Khan, F.S., Mughal, Z.U., Chakchouk, I., Lee, K., Rasheed, M., Hamza, R., Acharya, A., Ullah, E., et al. (2018). Novel candidate genes and variants underlying autosomal recessive neurodevelopmental disorders with intellectual disability. Hum Genet *137*, 735-752.

1548 18. Lek, M., Karczewski, K.J., Minikel, E.V., Samocha, K.E., Banks, E., Fennell, T.,
1549   O'Donnell-Luria, A.H., Ware, J.S., Hill, A.J., Cummings, B.B., et al. (2016). Analysis of
1550   protein-coding genetic variation in 60,706 humans. Nature *536*, 285-291.
1551 19. Mientjes, E.J., Willemsen, R., Kirkpatrick, L.L., Nieuwenhuizen, I.M., Hoogeveen-
1552   Westerveld, M., Verweij, M., Reis, S., Bardoni, B., Hoogeveen, A.T., Oostra, B.A., and
1553   Nelson, D.L. (2004). Fxr1 knockout mice show a striated muscle phenotype: implications
1554   for Fxr1p function in vivo. Human molecular genetics *13*, 1291-1302.
1555 20. Shen, M., Guo, Y., Dong, Q., Gao, Y., Stockton, M.E., Li, M., Kannan, S., Korabelnikov,
1556   T., Schoeller, K.A., Sirois, C.L., et al. (2021). FXR1 regulation of parvalbumin
1557   interneurons in the prefrontal cortex is critical for schizophrenia-like behaviors. Mol
1558   Psychiatry *26*, 6845-6867.
1559 21. Kang, J.Y., Wen, Z., Pan, D., Zhang, Y., Li, Q., Zhong, A., Yu, X., Wu, Y.C., Chen, Y.,
1560   Zhang, X., et al. (2022). LLPS of FXR1 drives spermiogenesis by activating translation of
1561   stored mRNAs. Science *377*, eabj6647.
1562 22. St Paul, A., Corbett, C., Peluzzo, A., Kelemen, S., Okune, R., Haines, D.S., Preston, K.,
1563   Eguchi, S., and Autieri, M.V. (2023). FXR1 regulates vascular smooth muscle cell
1564   cytoskeleton, VSMC contractility, and blood pressure by multiple mechanisms. Cell Rep
1565   *42*, 112381.
1566 23. Han, X., Zhou, Z., Fei, L., Sun, H., Wang, R., Chen, Y., Chen, H., Wang, J., Tang, H.,
1567   Ge, W., et al. (2020). Construction of a human cell landscape at single-cell level. Nature
1568   *581*, 303-309.
1569 24. Smith, J.A., Curry, E.G., Blue, R.E., Roden, C., Dundon, S.E.R., Rodriguez-Vargas, A.,
1570   Jordan, D.C., Chen, X., Lyons, S.M., Crutchley, J., et al. (2020). FXR1 splicing is
1571   important for muscle development and biomolecular condensates in muscle cells. The
1572   Journal of cell biology *219*.
1573 25. Chong, P.A., Vernon, R.M., and Forman-Kay, J.D. (2018). RGG/RG Motif Regions in
1574   RNA Binding and Phase Separation. J Mol Biol *430*, 4650-4665.
1575 26. Siomi, M.C., Zhang, Y., Siomi, H., and Dreyfuss, G. (1996). Specific sequences in the
1576   fragile X syndrome protein FMR1 and the FXR proteins mediate their binding to 60S
1577   ribosomal subunits and the interactions among them. Molecular and cellular biology *16*,
1578   3825-3832.
1579 27. Myrick, L.K., Hashimoto, H., Cheng, X., and Warren, S.T. (2015). Human FMRP
1580   contains an integral tandem Agenet (Tudor) and KH motif in the amino terminal domain.
1581   Human molecular genetics *24*, 1733-1740.
1582 28. Adinolfi, S., Ramos, A., Martin, S.R., Dal Piaz, F., Pucci, P., Bardoni, B., Mandel, J.L.,
1583   and Pastore, A. (2003). The N-terminus of the fragile X mental retardation protein
1584   contains a novel domain involved in dimerization and RNA binding. Biochemistry *42*,
1585   10437-10444.
1586 29. Thandapani, P., O'Connor, T.R., Bailey, T.L., and Richard, S. (2013). Defining the
1587   RGG/RG motif. Mol Cell *50*, 613-623.
1588 30. Hu, Y., Chen, Z., Fu, Y., He, Q., Jiang, L., Zheng, J., Gao, Y., Mei, P., Chen, Z., and
1589   Ren, X. (2015). The amino-terminal structure of human fragile X mental retardation
1590   protein obtained using precipitant-immobilized imprinted polymers. Nat Commun *6*,
1591   6634.
1592 31. Chen, T., Damaj, B.B., Herrera, C., Lasko, P., and Richard, S. (1997). Self-association
1593   of the single-KH-domain family members Sam68, GRP33, GLD-1, and Qk1: role of the
1594   KH domain. Molecular and cellular biology *17*, 5707-5718.
1595 32. Du, Z., Lee, J.K., Fenn, S., Tjhen, R., Stroud, R.M., and James, T.L. (2007). X-ray
1596   crystallographic and NMR studies of protein-protein and protein-nucleic acid interactions
1597   involving the KH domains from human poly(C)-binding protein-2. Rna *13*, 1043-1051.

1598   33.   Woolls, H.A., Lamanna, A.C., and Karbstein, K. (2011). Roles of Dim2 in ribosome
1599   assembly. J Biol Chem *286*, 2578-2586.
1600   34.   Garvanska, D.H., Alvarado, R.E., Mundt, F.O., Nilsson, E., Duel, J.K., Coscia, F.,
1601   Lindqvist, R., Lokugamage, K., Johnson, B.A., Plante, J.A., et al. (2023). SARS-CoV-2
1602   hijacks fragile X mental retardation proteins for efficient infection. bioRxiv,
1603   2023.2009.2001.555899.
1604   35.   Simm, D., Hatje, K., and Kollmar, M. (2015). Waggawagga: comparative visualization of
1605   coiled-coil predictions and detection of stable single α-helices (SAH domains).
1606   Bioinformatics *31*, 767-769.
1607   36.   Valcárcel, J., Gaur, R.K., Singh, R., and Green, M.R. (1996). Interaction of U2AF65 RS
1608   region with pre-mRNA branch point and promotion of base pairing with U2 snRNA
1609   [corrected]. Science *273*, 1706-1709.
1610   37.   Alex, D., and Lee, K.A. (2005). RGG-boxes of the EWS oncoprotein repress a range of
1611   transcriptional activation domains. Nucleic Acids Res *33*, 1323-1331.
1612   38.   Handa, N., Kukimoto-Niino, M., Akasaka, R., Kishishita, S., Murayama, K., Terada, T.,
1613   Inoue, M., Kigawa, T., Kose, S., Imamoto, N., et al. (2006). The crystal structure of
1614   mouse Nup35 reveals atypical RNP motifs and novel homodimerization of the RRM
1615   domain. J Mol Biol *363*, 114-124.
1616   39.   Mason, J.M., and Arndt, K.M. (2004). Coiled coil domains: stability, specificity, and
1617   biological implications. Chembiochem *5*, 170-176.
1618   40.   Chang, D.K., Cheng, S.F., Trivedi, V.D., and Lin, K.L. (1999). Proline affects
1619   oligomerization of a coiled coil by inducing a kink in a long helix. J Struct Biol *128*, 270-
1620   279.
1621   41.   Xu, Y., Huangyang, P., Wang, Y., Xue, L., Devericks, E., Nguyen, H.G., Yu, X., Oses-
1622   Prieto, J.A., Burlingame, A.L., Miglani, S., et al. (2021). ERα is an RNA-binding protein
1623   sustaining tumor cell survival and drug resistance. Cell *184*, 5215-5229.e5217.
1624   42.   Feng, Y., Absher, D., Eberhart, D.E., Brown, V., Malter, H.E., and Warren, S.T. (1997).
1625   FMRP associates with polyribosomes as an mRNP, and the I304N mutation of severe
1626   fragile X syndrome abolishes this association. Mol Cell *1*, 109-118.
1627   43.   Myrick, L.K., Nakamoto-Kinoshita, M., Lindor, N.M., Kirmani, S., Cheng, X., and Warren,
1628   S.T. (2014). Fragile X syndrome due to a missense mutation. Eur J Hum Genet *22*,
1629   1185-1189.
1630   44.   Zang, J.B., Nosyreva, E.D., Spencer, C.M., Volk, L.J., Musunuru, K., Zhong, R., Stone,
1631   E.F., Yuva-Paylor, L.A., Huber, K.M., Paylor, R., et al. (2009). A mouse model of the
1632   human Fragile X syndrome I304N mutation. PLoS Genet *5*, e1000758.
1633   45.   Hafner, M., Katsantoni, M., Köster, T., Marks, J., Mukherjee, J., Staiger, D., Ule, J., and
1634   Zavolan, M. (2021). CLIP and complementary methods. Nature Reviews Methods
1635   Primers *1*, 20.
1636   46.   Huang da, W., Sherman, B.T., and Lempicki, R.A. (2009). Systematic and integrative
1637   analysis of large gene lists using DAVID bioinformatics resources. Nature protocols *4*,
1638   44-57.
1639   47.   Vicente-Manzanares, M., Ma, X., Adelstein, R.S., and Horwitz, A.R. (2009). Non-muscle
1640   myosin II takes centre stage in cell adhesion and migration. Nature reviews. Molecular
1641   cell biology *10*, 778-790.
1642   48.   Hotulainen, P., and Hoogenraad, C.C. (2010). Actin in dendritic spines: connecting
1643   dynamics to function. The Journal of cell biology *189*, 619-629.
1644   49.   Newell-Litwa, K.A., Horwitz, R., and Lamers, M.L. (2015). Non-muscle myosin II in
1645   disease: mechanisms and therapeutic opportunities. Dis Model Mech *8*, 1495-1515.
1646   50.   Hall, A. (1998). Rho GTPases and the actin cytoskeleton. Science *279*, 509-514.
1647   51.   Riento, K., and Ridley, A.J. (2003). Rocks: multifunctional kinases in cell behaviour.
1648   Nature reviews. Molecular cell biology *4*, 446-456.

52. Amano, M., Ito, M., Kimura, K., Fukata, Y., Chihara, K., Nakano, T., Matsuura, Y., and Kaibuchi, K. (1996). Phosphorylation and activation of myosin by Rho-associated kinase (Rho-kinase). J Biol Chem *271*, 20246-20249.

53. Burridge, K., Fath, K., Kelly, T., Nuckolls, G., and Turner, C. (1988). Focal adhesions: transmembrane junctions between the extracellular matrix and the cytoskeleton. Annu Rev Cell Biol *4*, 487-525.

54. Sandquist, J.C., Swenson, K.I., Demali, K.A., Burridge, K., and Means, A.R. (2006). Rho kinase differentially regulates phosphorylation of nonmuscle myosin II isoforms A and B during cell rounding and migration. J Biol Chem *281*, 35873-35883.

55. Tojkander, S., Gateva, G., and Lappalainen, P. (2012). Actin stress fibers--assembly, dynamics and biological roles. J Cell Sci *125*, 1855-1864.

56. Zhang, J., Ma, Y., Taylor, S.S., and Tsien, R.Y. (2001). Genetically encoded reporters of protein kinase A activity reveal impact of substrate tethering. Proc Natl Acad Sci U S A *98*, 14997-15002.

57. Gullberg, M., Gústafsdóttir, S.M., Schallmeiner, E., Jarvius, J., Bjarnegård, M., Betsholtz, C., Landegren, U., and Fredriksson, S. (2004). Cytokine detection by antibody-based proximity ligation. Proc Natl Acad Sci U S A *101*, 8420-8424.

58. Irwin, S.A., Patel, B., Idupulapati, M., Harris, J.B., Crisostomo, R.A., Larsen, B.P., Kooy, F., Willems, P.J., Cras, P., Kozlowski, P.B., et al. (2001). Abnormal dendritic spine characteristics in the temporal and visual cortices of patients with fragile-X syndrome: a quantitative examination. Am J Med Genet *98*, 161-167.

59. He, C.X., and Portera-Cailliau, C. (2013). The trouble with spines in fragile X syndrome: density, maturity and plasticity. Neuroscience *251*, 120-128.

60. Le Hir, H., Saulière, J., and Wang, Z. (2016). The exon junction complex as a node of post-transcriptional networks. Nature reviews. Molecular cell biology *17*, 41-54.

61. Athar, Y.M., and Joseph, S. (2020). RNA-Binding Specificity of the Human Fragile X Mental Retardation Protein. J Mol Biol *432*, 3851-3868.

62. Singh, R., and Valcárcel, J. (2005). Building specificity with nonspecific RNA-binding proteins. Nat Struct Mol Biol *12*, 645-653.

63. Bonneau, F., Basquin, J., Steigenberger, B., Schäfer, T., Schäfer, I.B., and Conti, E. (2023). Nuclear mRNPs are compact particles packaged with a network of proteins promoting RNA-RNA interactions. Genes Dev *37*, 505-517.

64. Pawson, T., and Scott, J.D. (1997). Signaling through scaffold, anchoring, and adaptor proteins. Science *278*, 2075-2080.

65. Lajoie, P., Goetz, J.G., Dennis, J.W., and Nabi, I.R. (2009). Lattices, rafts, and scaffolds: domain regulation of receptor signaling at the plasma membrane. The Journal of cell biology *185*, 381-385.

66. Chen, X., and Mayr, C. (2022). A working model for condensate RNA-binding proteins as matchmakers for protein complex assembly. RNA *28*, 76-87.

67. Miller, J.D., Ganat, Y.M., Kishinevsky, S., Bowman, R.L., Liu, B., Tu, E.Y., Mandal, P.K., Vera, E., Shim, J.W., Kriks, S., et al. (2013). Human iPSC-based modeling of late-onset disease via progerin-induced aging. Cell Stem Cell *13*, 691-705.

68. Concordet, J.P., and Haeussler, M. (2018). CRISPOR: intuitive guide selection for CRISPR/Cas9 genome editing experiments and screens. Nucleic Acids Res *46*, W242-w245.

69. Walton, R.T., Christie, K.A., Whittaker, M.N., and Kleinstiver, B.P. (2020). Unconstrained genome targeting with near-PAMless engineered CRISPR-Cas9 variants. Science *368*, 290-296.

70. Clement, K., Rees, H., Canver, M.C., Gehrke, J.M., Farouni, R., Hsu, J.Y., Cole, M.A., Liu, D.R., Joung, J.K., Bauer, D.E., and Pinello, L. (2019). CRISPResso2 provides accurate and rapid genome editing sequence analysis. Nat Biotechnol *37*, 224-226.

1700　71.　Hwang, G.H., Jeong, Y.K., Habib, O., Hong, S.A., Lim, K., Kim, J.S., and Bae, S. (2021).
1701　　　　PE-Designer and PE-Analyzer: web-based design and analysis tools for CRISPR prime
1702　　　　editing. Nucleic Acids Res *49*, W499-W504.
1703　72.　van der Walt, S., Schonberger, J.L., Nunez-Iglesias, J., Boulogne, F., Warner, J.D.,
1704　　　　Yager, N., Gouillart, E., Yu, T., and scikit-image, c. (2014). scikit-image: image
1705　　　　processing in Python. PeerJ *2*, e453.
1706　73.　Navarrete-Perea, J., Yu, Q., Gygi, S.P., and Paulo, J.A. (2018). Streamlined Tandem
1707　　　　Mass Tag (SL-TMT) Protocol: An Efficient Strategy for Quantitative (Phospho)proteome
1708　　　　Profiling Using Tandem Mass Tag-Synchronous Precursor Selection-MS3. J Proteome
1709　　　　Res *17*, 2226-2236.
1710　74.　Rappsilber, J., Mann, M., and Ishihama, Y. (2007). Protocol for micro-purification,
1711　　　　enrichment, pre-fractionation and storage of peptides for proteomics using StageTips.
1712　　　　Nature protocols *2*, 1896-1906.
1713　75.　Lee, F.C.Y., Chakrabarti, A.M., Hänel, H., Monzón-Casanova, E., Hallegger, M., Militti,
1714　　　　C., Capraro, F., Sadée, C., Toolan-Kerr, P., Wilkins, O., et al. (2021). An improved iCLIP
1715　　　　protocol. bioRxiv, 2021.2008.2027.457890.
1716　76.　Zarnegar, B.J., Flynn, R.A., Shen, Y., Do, B.T., Chang, H.Y., and Khavari, P.A. (2016).
1717　　　　irCLIP platform for efficient characterization of protein-RNA interactions. Nat Methods
1718　　　　*13*, 489-492.
1719　77.　Meszaros, B., Erdos, G., and Dosztanyi, Z. (2018). IUPred2A: context-dependent
1720　　　　prediction of protein disorder as a function of redox state and protein binding. Nucleic
1721　　　　Acids Res *46*, W329-W337.
1722　78.　Huerta-Cepas, J., Szklarczyk, D., Forslund, K., Cook, H., Heller, D., Walter, M.C., Rattei,
1723　　　　T., Mende, D.R., Sunagawa, S., Kuhn, M., et al. (2016). eggNOG 4.5: a hierarchical
1724　　　　orthology framework with improved functional annotations for eukaryotic, prokaryotic and
1725　　　　viral sequences. Nucleic Acids Res *44*, D286-293.
1726　79.　Waterhouse, A.M., Procter, J.B., Martin, D.M., Clamp, M., and Barton, G.J. (2009).
1727　　　　Jalview Version 2--a multiple sequence alignment editor and analysis workbench.
1728　　　　Bioinformatics *25*, 1189-1191.
1729　80.　Morales, J., Pujar, S., Loveland, J.E., Astashyn, A., Bennett, R., Berry, A., Cox, E.,
1730　　　　Davidson, C., Ermolaeva, O., Farrell, C.M., et al. (2022). A joint NCBI and EMBL-EBI
1731　　　　transcript set for clinical genomics and research. Nature *604*, 310-315.
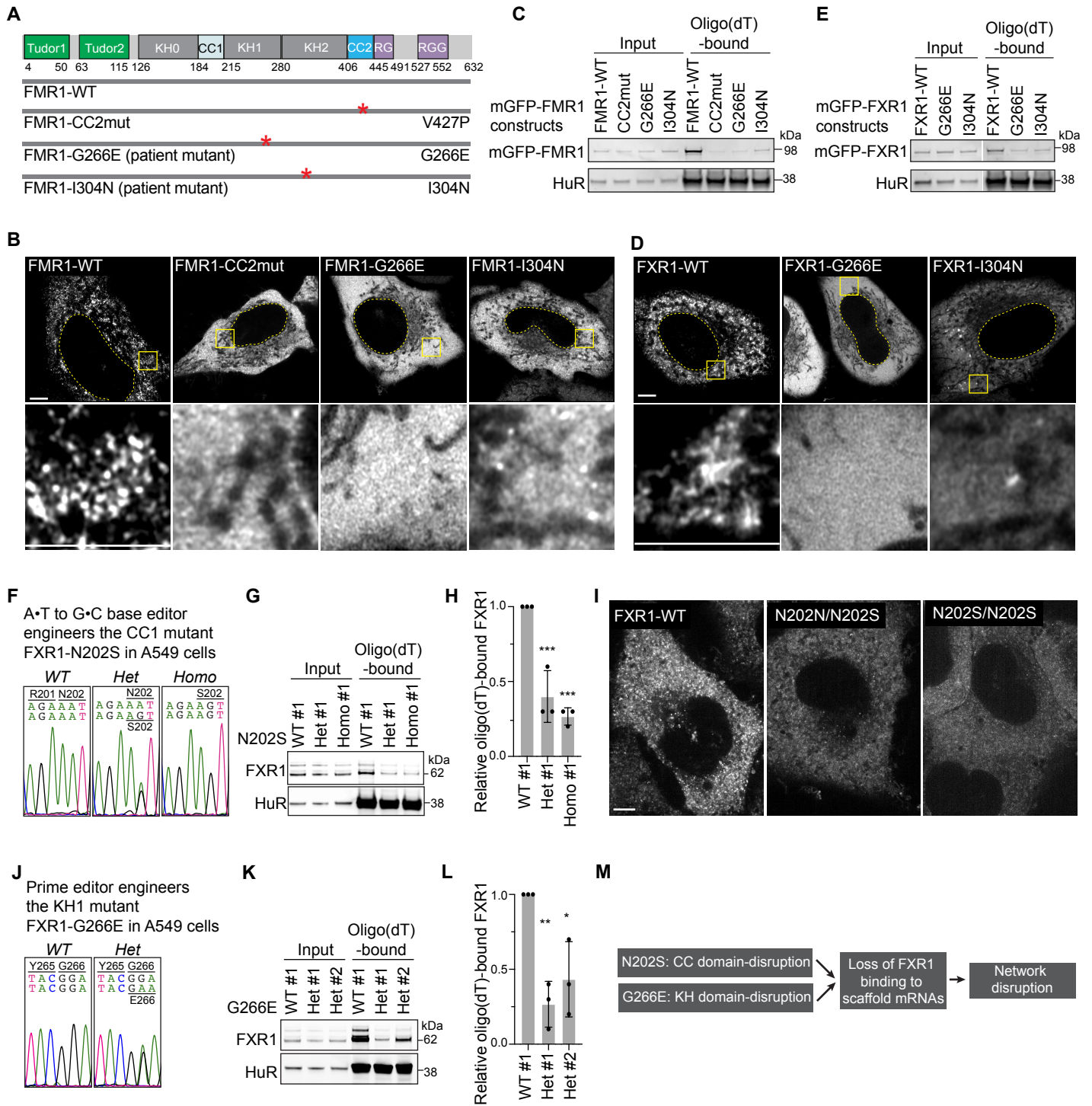
1732

Figure 1

Figure 2
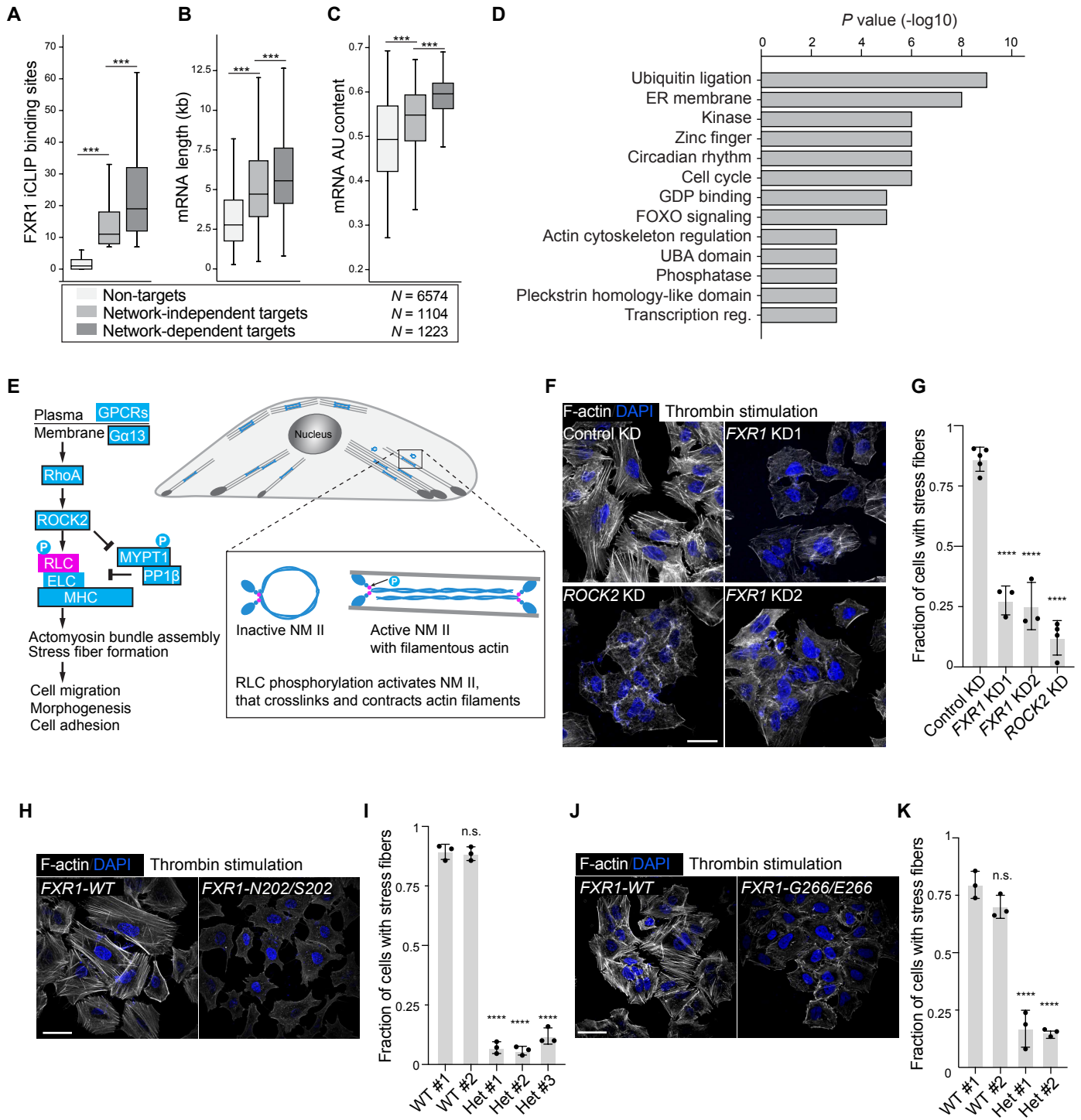
Figure 3

Figure 4

Figure 5
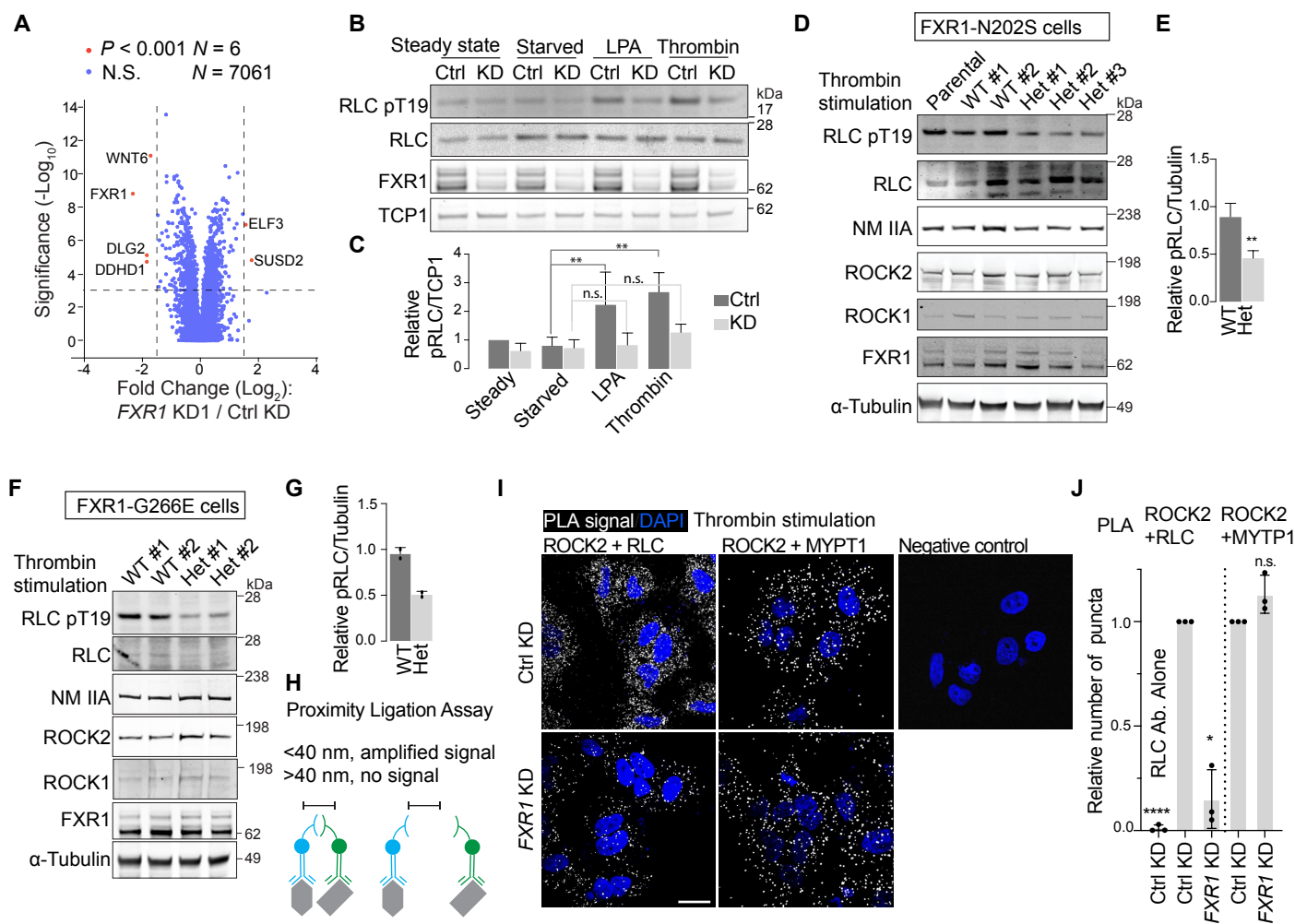
Figure 6
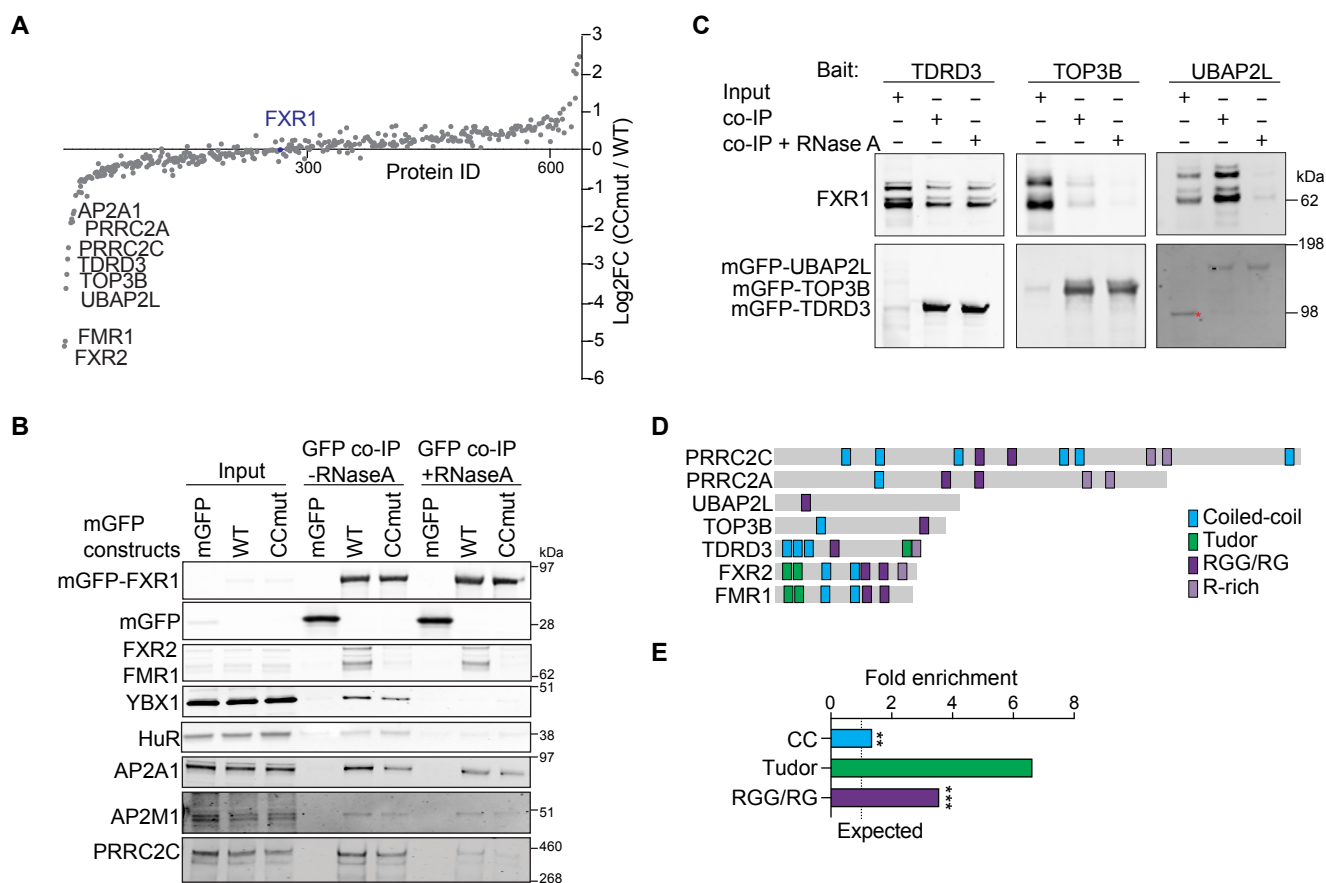
Figure 7

Figure S1

Figure S2

A

FXR1-a [NP_005078.2]   sh3 ... sh5 ... sh7 ... 621 AA

FXR1-b [NP_001013456.1]   539 AA

HPA018246   HPA055475

B

exon 14   exon 16

FXR1-a 411-VLKDPDSNPYSLLDNTESDQTADTDASESHHSTNRRRRSRRRRTDEDAVLMDGMTESDTASVNENGLVTVADYISRA-544
FXR1-b 411-VLKDPDSNPYSLLDNTESDQTADTDASESHHSTNRRRRSRRRRTDEDAVLMDGMTESDTASVNENGL----------534

exon 17

FXR1-a 545-ESQSRQRNLPRETLAKNKKEMAKDVIEEHGPSEKAINGPTSASGDDISKLQRTPGEEKINTLKEENTQEAAVLNGVS-621
FXR1-b 535---------------------GKRCD---539

C

D

E

F

Figure S3

Figure S4

Figure S5

A

mGFP-FXR1-WT	-	-	+	-
mGFP-FXR1-CC2mut	-	-	-	+
FXR1 KD	-	+	+	+
Ctrl KD	+	-	-	-

kDa
— 97 mGFP-FXR1
Endogenous FXR1
— 64
— 51
— 39 GAPDH

B

WT   CC2mut

kDa
-130
-100
-70

C

- CDS 46.8 %
- 3′UTR 50.6 %
- 5′UTR 2.6 %

D

| | Input | Flow-through | | Elution | |
| | | FXR1 | IgG | FXR1 | IgG |

kDa
FXR1
-62

E

FXR1 binding sites | RNA-IP qPCR ■ FC (FXR1/IgG)

	WT	CC2mut	
Non-targets	0	0	MYL9
	4	7	TCP1
	5	6	ROCK1
Network-independent target	19	14	PPP1R12A
Network-dependent targets	20	6	CDK1
	20	9	UBE3C
	21	5	UBE4A
	23	4	FBXO45
	27	5	LATS1
	27	6	NEDD4
	33	12	JAK1
	39	17	SLK
	44	8	PAK2
	51	8	PIK3C2A
	55	12	UBE2K
	56	16	PRKAA1
	60	14	MET
	61	7	CBL
	80	14	ROCK2
	90	34	WNK1
	97	28	IQGAP1
	133	18	MDM2
	550	113	TGFBR1

0.5 1 2 4 8 16 32 64
Fold change (FXR1/IgG)

F

FC FXR1 binding sites (WT/CC2mut)
8 7 6 5 4 3 2 1 0
****

G

3′UTR length (kb)
8 6 4 2 0
*** ***

- Non-targets — N = 6574
- Network-independent targets — N = 1104
- Network-dependent targets — N = 1223

Figure S6

Cell signaling Technologies 3672

Abcam ab125025

Novus Biologicals H00009475-M02

Figure S7

A

B

ROCK2-FL
ROCK2-N
ROCK2-C

C

D

E

Coiled-coil	EPVKRGNDTDVRRKEKENRKLHMELKSEREKLTQQMIKYQKELNEMQAQIAEESQIRIELQMTLD SKDSDIEQLRSQLQALHIGLDSSSIGSGPGDAEADDGFP
RGG	RGGPGRRQGRGRGRARRPPGKPNPRRPK
Tudor	MWKPGDECFALYWEDNKFYRAEVEALHSSGMTAVVKFIDYGNYEEVLLSNIKPIQTEAWEEE
R-rich	GTYDQTLEFRRGGDGQPRRSTRPTQQFYQPPRARN
Tudor-R-rich	MWKPGDECFALYWEDNKFYRAEVEALHSSGMTAVVKFIDYGNYEEVLLSNIKPIQTEAWEEE GTYDQTLEFRRGGDGQPRRSTRPTQQFYQPPRARN